

Technical Report

DESIGN OF AN AUV RECHARGING SYSTEM

Bryan D. Miller

MITSG 05-6TH

MIT Sea Grant College Program



Massachusetts Institute
of Technology
Cambridge, Massachusetts
02139

DESIGN OF AN AUV RECHARGING SYSTEM

Bryan D. Miller

MITSG 05-6TH

Sea Grant College Program
Massachusetts Institute of Technology
Cambridge, Massachusetts 02139

NOAA Grant No.: NA16RG2255

Design of an AUV Recharging System

By

Bryan D. Miller

B.S. Electrical Engineering

The Citadel, 1999

Submitted to the Department of Ocean Engineering and the Department of Electrical Engineering and Computer Science in Partial Fulfillment of the Requirements for the Degrees of

Naval Engineer

and

Master of Science in Electrical Engineering

at the

Massachusetts Institute of Technology

June 2005

© 2005 Massachusetts Institute of Technology. All rights reserved.

MIT hereby grants to the US Government permission to reproduce and to distribute publicly paper and electronic copies of this thesis document in whole or in part.

Signature of Author _____
Department of Ocean Engineering and the
Department of Electrical Engineering and Computer Science
May 19, 2005

Certified by _____
Chryssostomos Chryssostomidis
Henry L. and Grace Doherty Professor of Ocean Science and Engineering
Thesis Supervisor

Certified by _____
James L. Kirtley
Professor of Electrical Engineering
Thesis Reader

Accepted by _____
Michael Triantafyllou
Professor of Ocean Engineering
Chair, Departmental Committee on Graduate Students

Accepted by _____
Arthur C. Smith, Professor of Electrical Engineering and Computer Science
Chairman, Department Committee on Graduate Students
Department of Electrical Engineering and Computer Science

Design of an AUV Recharging System

by
Bryan D. Miller

Submitted to the Department of Ocean Engineering and the Department of Electrical Engineering and Computer Science in Partial Fulfillment of the Requirements for the Degrees of

Naval Engineer

and

Master of Science in Electrical Engineering

ABSTRACT

The Odyssey AUV Series uses a Lithium-ion Polymer battery which is able to supply the necessary power for a limited mission time. The current method of recharge includes surfacing the AUV, opening the vehicle, removing the battery from the vehicle and recharging the battery. A different approach is proposed which uses an inductive coupler and power electronics to conduct a battery charge without opening the vehicle or removing the battery.

Thesis Supervisor: Chrysostomos Chrysostomidis

Title: Henry L. and Grace Doherty Professor of Ocean Science and Engineering

Thesis Reader: James L. Kirtley

Title: Professor of Electrical Engineering

Table of Contents

| | |
|--|----|
| List of Figures..... | 5 |
| List of Tables..... | 6 |
| Chapter 1 Introduction..... | 7 |
| 1.1 Purpose/Problem..... | 7 |
| 1.2 Background..... | 7 |
| 1.3 Proposed Solution..... | 9 |
| Chapter 2 Theory..... | 13 |
| 2.1 Inductive Coupler..... | 13 |
| 2.1.1 Magnetizing Inductance..... | 19 |
| 2.1.2 Leakage Inductance..... | 21 |
| 2.1.3 Copper Losses..... | 22 |
| 2.1.4 Core Losses..... | 23 |
| 2.2 Power Electronics..... | 25 |
| 2.2.1 AC to AC Converter..... | 25 |
| 2.2.2 AC to DC Converter..... | 32 |
| Chapter 3 Modeling and Simulation..... | 35 |
| 3.1 Inductive Coupler..... | 35 |
| 3.2 Circuit Simulation..... | 44 |
| Chapter 4 Prototype Results..... | 48 |
| 4.1 Secondary Circuit..... | 48 |
| 4.2 Primary Circuit..... | 52 |
| Chapter 5 Conclusions..... | 55 |
| Acknowledgements..... | 56 |
| List of References..... | 57 |

List of Figures

| | |
|---|----|
| Figure 1: AUV Power Supply (Normal, Underway, Not Charging) | 8 |
| Figure 2: Current Battery Charge Scheme..... | 9 |
| Figure 3: Proposed Charging Scheme..... | 10 |
| Figure 4: Functional Block Diagram | 11 |
| Figure 5: Basic System Diagram | 12 |
| Figure 6: (a) Complete Equivalent Circuit for a Pulse Transformer (b) Alternate Form of Complete Equivalent Circuit for a Pulse Transformer [1]..... | 18 |
| Figure 7: Simplified IEEE Equivalent Circuit [1] | 18 |
| Figure 8: Full-Wave Bridge Rectifier | 26 |
| Figure 9: Input Waveform (Full-Wave Bridge Rectifier)..... | 26 |
| Figure 10: Output Waveform Added to Figure 9..... | 27 |
| Figure 11: Smoothing Capacitor Added to Figure 8..... | 28 |
| Figure 12: Input/Output Waveform with Added Smoothing Capacitor | 28 |
| Figure 13: Half-bridge Circuit Diagram | 29 |
| Figure 14: Half-bridge Waveforms..... | 30 |
| Figure 15: Full-bridge (H-bridge) Circuit Diagram..... | 31 |
| Figure 16: Full-bridge Waveforms | 31 |
| Figure 17: Full-bridge Output Waveform..... | 32 |
| Figure 18: DC to DC (Buck) Converter..... | 33 |
| Figure 19: Buck Converter Waveforms..... | 34 |
| Figure 20: Primary Losses vs. Primary Turns | 36 |
| Figure 21: Inductive Coupler Cross-section (Shown with Primary Core Exposed)..... | 38 |
| Figure 22: Inductive Coupler (One-half of Secondary) Dimensions (Shown in mm)..... | 38 |
| Figure 23: Top View of Primary ("Puck")..... | 39 |
| Figure 24: Side View of Secondary (Note Split Windings) | 39 |
| Figure 25: Back View of Secondary (Note Split Windings) | 40 |
| Figure 26: Front View with Primary Being Inserted | 40 |
| Figure 27: Front View with Primary Inserted..... | 41 |
| Figure 28: Inductive Coupler Parameters (Similar to Figure 7), Shown in Open Circuit | 42 |
| Figure 29: Inductive Coupler Parameters with Secondary Components Transformed | 43 |
| Figure 30: Simulation Circuit: $I_{\text{CHARGE}} = 15\text{A}$ | 45 |
| Figure 31: Simulation: $I_{\text{CHARGE}} = 15\text{A}$, $dI_L=104\text{mA}$, $dI_{\text{CHARGE}}=102\text{mA}$ | 46 |
| Figure 32: Simulation: $I_{\text{CHARGE}}=15\text{A}$, $dV_O=52\text{mV}$ | 47 |
| Figure 33: Secondary Circuit..... | 49 |
| Figure 34: MOSFET Driver Circuitry [4]..... | 50 |
| Figure 35: MOSFET Driver Input and Output Waveforms: $V_{\text{in}}=6.2\text{VDC}$, $V_{\text{out}}=2.26\text{V}$, $d=0.5$. | 51 |
| Figure 36: MOSFET Driver Input and "Buck" Converter Output Waveforms: $V_{\text{in}}=6.2\text{VDC}$, $V_{\text{out}}=2.26\text{V}$, $d=0.5$ | 51 |
| Figure 37: MOSFET Driver Input and "Buck" Converter Output Waveforms: $V_{\text{in}}=12.7\text{VDC}$, $V_{\text{out}}=9.2\text{V}$, $d=0.8$ | 52 |
| Figure 38: Primary Circuit..... | 53 |

| | |
|--|----|
| Figure 39: Primary MOSFET Driver High Output..... | 54 |
| Figure 40: Inductive Coupler Output (M = CH1 - CH2)..... | 54 |

List of Tables

| | |
|--|----|
| Table 1: Properties of Soft Magnetic Materials [6]..... | 14 |
| Table 2: Material Properties for Magnetics Ferrites [9]..... | 15 |
| Table 3: Core Loss Factors [9]..... | 25 |
| Table 4: Core Parameters vs. Primary Turns..... | 37 |
| Table 5: Inductive Coupler HP 4192A LF Impedance Analyzer Results..... | 42 |
| Table 6: Inductive Coupler Characteristics..... | 44 |

Chapter 1 Introduction

1.1 Purpose/Problem

The Odyssey AUV (Autonomous Underwater Vehicle) Series uses a Lithium-ion Polymer battery which is able to supply the necessary power for a limited mission time. The current method of recharge includes surfacing the AUV, opening the vehicle, removing the battery from the vehicle and recharging the battery. A different approach is proposed which uses an inductive coupler and power electronics to conduct a battery charge without opening the vehicle or removing the battery.

1.2 Background

The Odyssey Series AUV uses a Lithium-ion Polymer battery which is removed from the vehicle in order to perform a battery charge. Many man-hours are spent once the vehicle is surfaced to remove the vehicle from the water, open the vehicle and subsequently remove the battery from the vehicle for charging. A more efficient means of charging the batteries is desired. The most obvious choice is to charge the battery by any means which includes maintaining the battery in the vehicle, and the vehicle closed, during the charge.

“Design of an AUV Recharging System” [2] focused on the design of an inductive coupler that could be used to charge multiple vehicles from the same primary winding using a Linear Coaxial-Wound Transformer (LCWT). The coupler portion of Gish’s research was based primarily on “Contactless Underwater Power Delivery” [3] and “Inductive Couplers in Underwater Power Distribution Networks – Improving Their Applicability” [1]. However, [2] did not take into account the actual charging scheme and focused electrically on the method of power transfer, the inductive coupler.

Figure 1 depicts the current method used during normal, underway operation. All the components shown in Figure 1 are located inside the AUV. The battery is connected to the main bus where voltage is maintained at 28-34 VDC. The Main Vehicle Computer (MVC) is powered from this main bus through a DC/DC converter to approximately the same voltage. A second connector also connects directly to the main bus, but does not provide power during the in-water operation.

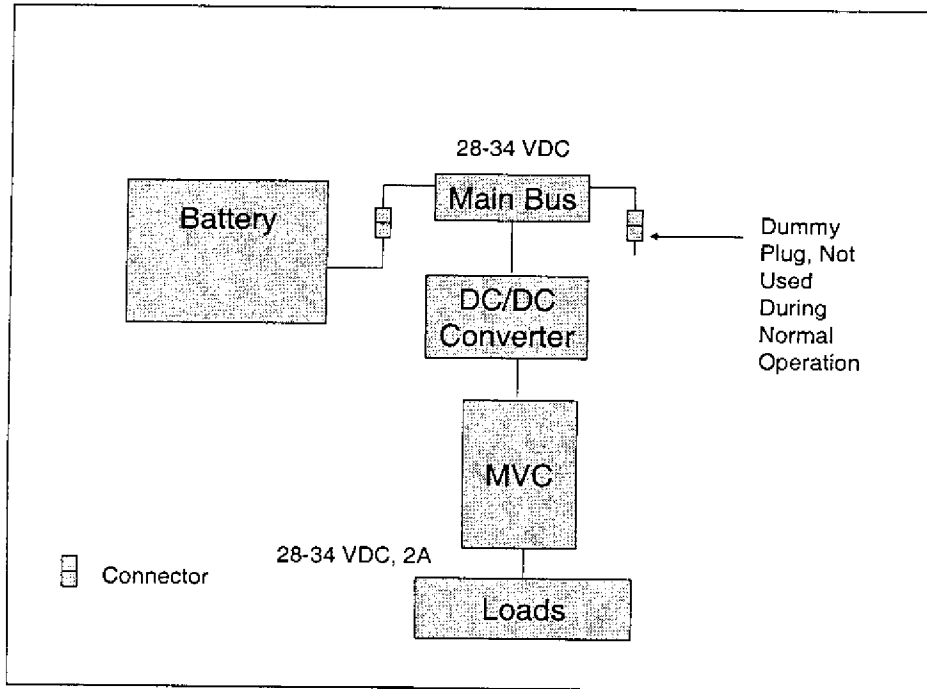


Figure 1: AUV Power Supply (Normal, Underway, Not Charging)

Currently during a battery charge, Figure 2 (shown with dashed lines), a total of three connections are made. The first connector (call this the “battery connector”) is unplugged from the main bus and subsequently connected to the charging power supply (Charger). In addition, an RS-485 connection (call this the “communication connector”) is made which allows the Charging Computer to communicate with the battery to monitor the State of Charge (SoC). During the charge, a second DC power supply is connected to the main bus to provide power to

the AUV loads and MVC (call this the “in-charge connector”). A diode restricts the flow of power to one direction – from the DC power supply to the main bus.

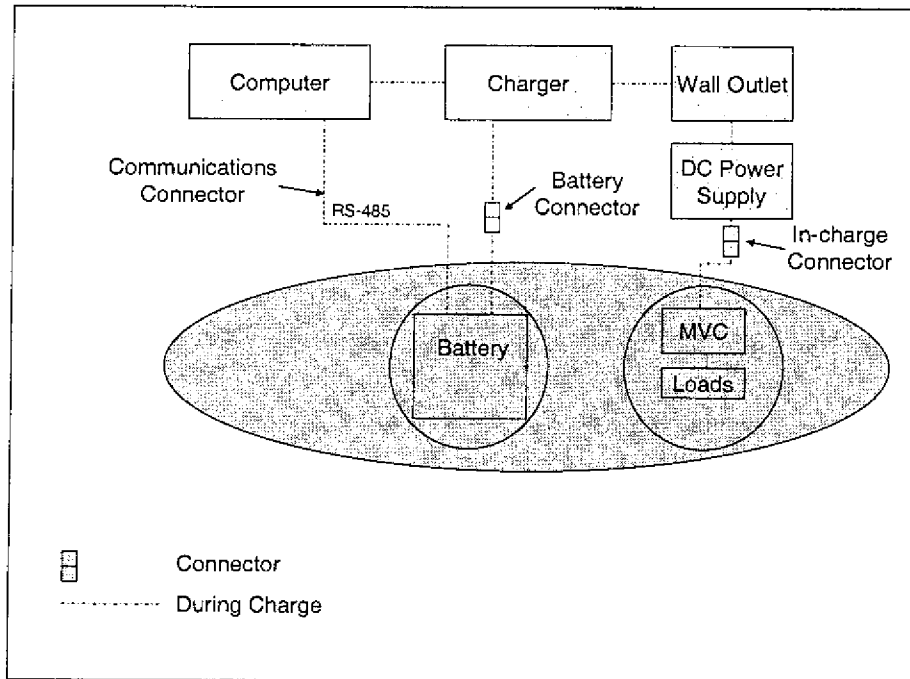


Figure 2: Current Battery Charge Scheme

1.3 Proposed Solution

The proposed charging scheme utilizes the connectors that are currently installed, but will make some modifications to the vehicle. Figure 3 and Figure 4 show the proposed scheme and are described below. The battery will remain connected to the main bus via the “battery connector.” The “in-charge connector” is now connected to the output of the DC/DC converter (from the inductive coupler) or alternatively to the DC Power Supply (as before, shown in Figure 2). The DC/DC converter will be placed between the “in-charge connector” and the main bus in order to control the bus voltage and current which is applied to the battery for charging.

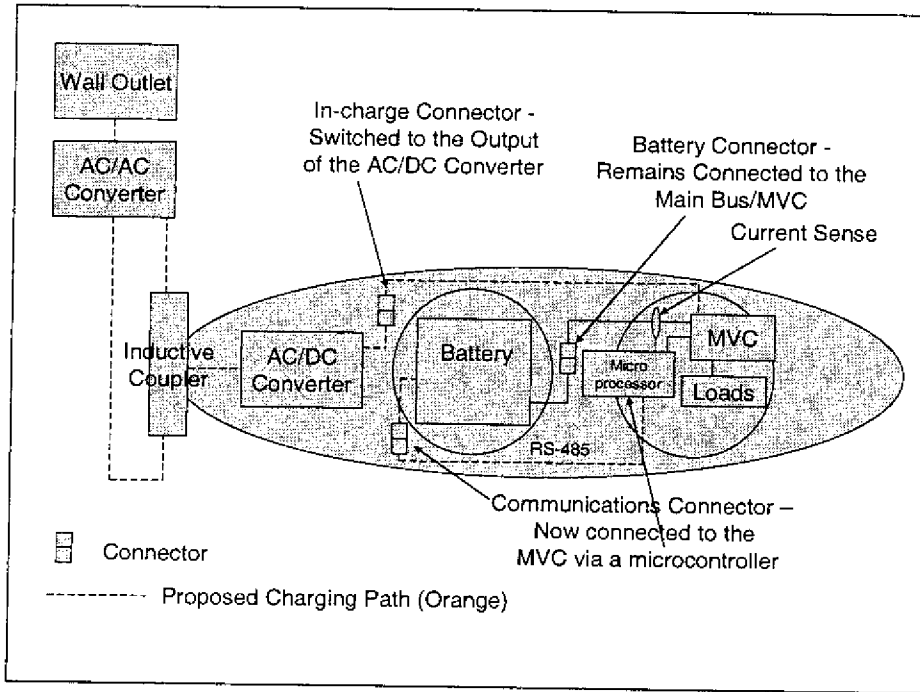


Figure 3: Proposed Charging Scheme

The charging sequence will be controlled by using a microprocessor to control the duty ratio of the DC/DC converter. The microprocessor will use the voltage readings from the battery (through the MVC) and a yet to be installed current sensor (in-line with the battery). Because it is a Lithium-ion Polymer battery, it is imperative that the voltage of each of the cells, the charge current and the temperature of the battery be monitored and controlled, as necessary.

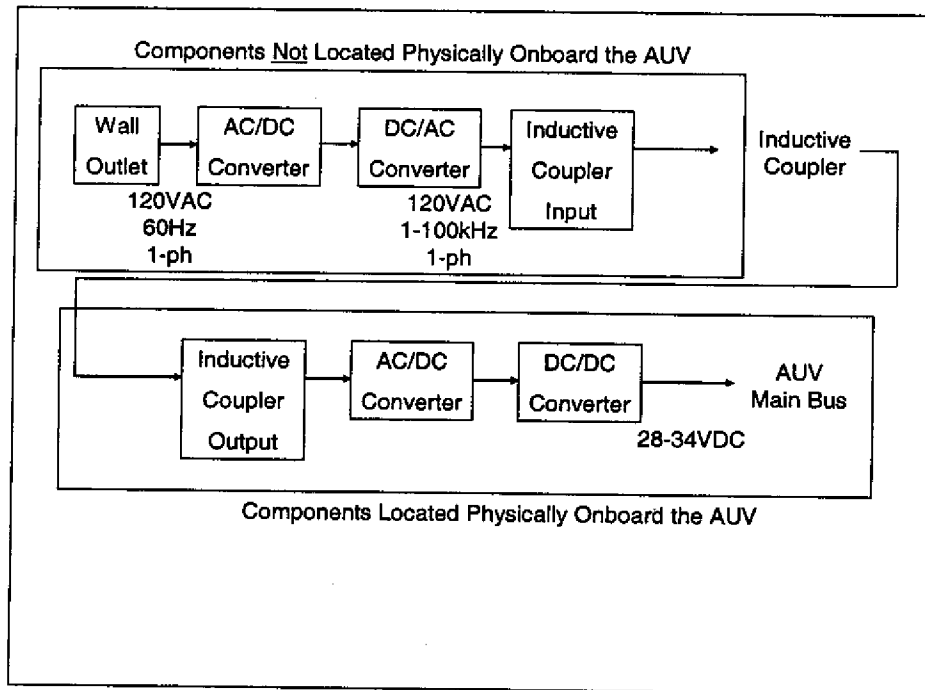


Figure 4: Functional Block Diagram

Chapter 2 describes in detail the theory associated with those components listed in Figure 4. The AC/DC converter is used to convert the 120VAC, 60Hz, single phase power to a relatively constant DC value. The DC signal is then converted back to a 1 to 100 kHz signal in order to minimize the size of the inductive coupler. In general, as the frequency of operation increases, the size of the components decreases. All the components listed to this point will be located in a power box or other means that will be kept off the AUV. This minimizes the weight of the AUV and thus less weight compensation will be required for the added hardware.

A portion of the recharge system will be kept onboard the AUV. The inductive coupler is a transformer and transforms the 1 to 100 kHz input signal from a nominal voltage of 120 VAC to a nominal voltage necessary to power the secondary side electronics. It is anticipated that the secondary side will power the normal AUV loads, via the Main Bus, in addition to charging the battery.

The AUV loads are expected to be 2A at main bus voltage (28-34 VDC), or approximately 70W. The recharging current is expected to be between 15A to 5A (or 0A when connected, but not charging), with voltage of 28-34 VDC. This results in a power output to the battery charge of approximately 510W. Therefore, total output power during an anticipated charge is 580W (maximum). This number accounts for the present loading of the AUV. Therefore, the recharge system will be designed to power at least 700W for future consideration. Figure 5 shows a basic schematic diagram of the solution proposed. The dotted line indicates the boundary of the vehicle.

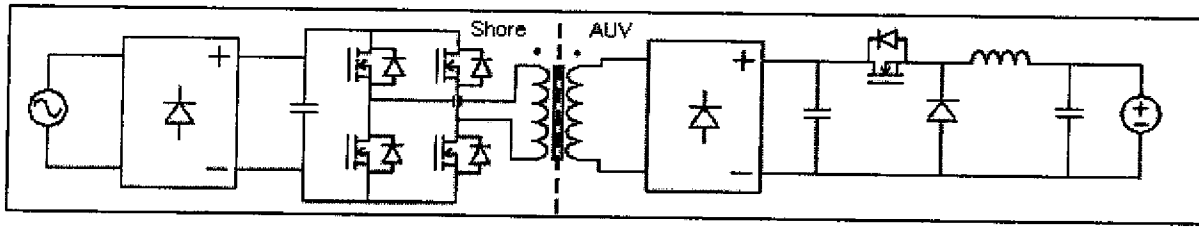


Figure 5: Basic System Diagram

Chapter 2 Theory

The concept in Chapter 1 is continued here by developing the major components of the AUV recharging system. Each of the major subsystems will contain its own heading and the theory behind the operation of that subsystem will be explained.

2.1 Inductive Coupler

The inductive coupler is a modified form of transformer. It can be used to step up or step down voltage, just as a transformer could be used. However, one of the main uses of inductive couplers is to replace conductive couplers, or plugs, in electric power systems. One example of this is the Electric Vehicle Charger used to recharge electric vehicles. The reason for replacing conductive couplers in this environment is to avoid galvanic coupling which is problematical because of salt water (safety, corrosion, etc.). Rhodes [10] describes the fundamental concepts behind a power transformer and the associated conclusions about the design process when a separable core is present.

Before attempting to model the inductive coupler, it must be determined what type of material will be used. "A Critical Comparison of Ferrites with Other Magnetic Materials," [6] compares many of the commercially available soft magnetic materials. This comparison is listed in Table 1. Based on the frequency range of interest, low core cost, and low core losses, a ferrite core was chosen. Ferrites are dense, homogenous ceramic structures made by mixing iron oxide with oxides or carbonates of one or more metals such as zinc, manganese, nickel or magnesium. They are pressed, then fired in a kiln at 2000°F, and machined as needed to meet various operational requirements. Ferrite parts can be easily and economically molded into different geometries. Many diverse materials are available, providing many choices of desirable

electrical and mechanical properties. The ferrites used by Magnetics are the manganese-zinc type used for communications (frequencies from 1 kHz to 1000 kHz) and for power applications such as in Switching Mode Power Supplies (SMPS).

Table 1: Properties of Soft Magnetic Materials [6]

| Material | Initial Perm. μ_0 | B_{max} Kilogausses | Loss Coefficients | | | Curie Temp. °C | Resistivity (ohm-cm) | $\mu_0 Q$ at 100 kHz | Operating Frequencies |
|------------------------------|-----------------------|-----------------------|-------------------|-----------------|-----------------|----------------|----------------------|----------------------|-----------------------|
| | | | $e \times 10^6$ | $a \times 10^3$ | $c \times 10^3$ | | | | |
| Fe | 250 | 22 | - | - | - | 770 | 10×10^{-6} | - | 60-1000 Hz |
| Si-Fe (unoriented) | 400 | 20 | 670 | 120 | 75 | 740 | 50×10^{-6} | - | 60-1000 Hz |
| Si-Fe (oriented) | 1500 | 20 | - | - | - | 740 | 50×10^{-6} | - | 60-1000Hz |
| 50-50 Ni Fe (grain-oriented) | 2000 | 16 | - | - | - | 360 | 40×10^{-6} | - | 60-1000Hz |
| 79 Permalloy | 12,000 to 100,000 | 8 to 11 | 173 | - | - | 450 | 55×10^{-6} | 8000 to 12,000 | 1 kHz-75kHz |
| AMORPHOUS Alloy B | 3000 | 15-16 | - | - | - | 370 | 135×10^{-6} | - | to 250 kHz |
| AMORPHOUS Alloy E | 20,000 | 5-6.5 | - | - | - | 205 | 140×10^{-6} | - | to 250 kHz |
| Permalloypowder | 14 to 550 | 3 | .01 to .04 | .002 | .05 to .1 | 450 | 1. | 10,000 | 10 kHz-1 MHz |
| High Flux powder | 14 to 160 | 15 | - | - | - | 360 | - | - | 10 kHz to 1 MHz |
| Kool Mu® powder | 26 to 125 | 10 | - | - | - | 740 | - | - | to 10 MHz |
| Iron powder | 5 to 80 | 10 | .002 to .04 | .002 to .4 | .2 to 1.4 | 770 | 10^6 | 2000 to 30,000 | 100 kHz-100 MHz |
| Ferrite-MnZn | 750 to 15,000 | 3 to 5 | .001 | .002 | .01 | 100 to 300 | 10 to 100 | 100,000 to 500,000 | 10 kHz-2 MHz |
| Ferrite-NiZn | 10 to 1500 | 3 to 5 | - | - | - | 150 to 450 | 10^6 | 30,000 | 200 kHz-100MHz |
| Co-Fe 50% | 800 | 24 | - | - | - | 980 | 70×10^{-6} | - | - |

Magnetics also provides a breakdown of the material properties of their ferrite cores in [9]. Those properties are included in Table 2.

Table 2: Material Properties for Magnetics Ferrites [9]

| | | | INDUCTORS & POWER TRANSFORMERS | | | EMI/RFI FILTERS & BROADBAND TRANSFORMERS | | |
|---|---------------------------------|------------------------------------|--------------------------------|--------------------------|-------------------|--|--------------|--------------|
| | | | R | P | F | J | W | H |
| Initial Permeability | μ_i | — | 2,300 ± 25% | 2,500 ± 25% | 3,000 ± 20% | 5,000 ± 20% | 10,000 ± 30% | 15,000 ± 30% |
| Maximum Usable Frequency (50% roll-off) | f | MHz | <1.5 | <1.2 | <1.3 | <1 | <0.25 | <0.15 |
| Relative Loss Factor | $\frac{\tan \delta}{\mu_{loc}}$ | 10^{-6} | | | <8 (100kHz) | <20 (100kHz) | <7 (10kHz) | <15 (10kHz) |
| * Curio Temperature | T_c | °C | >230 | >230 | >250 | >140 | >125 | >120 |
| * Relative Temp. Factor -30°C to +20°C +20°C to 70°C | /°C | $10^{-6}/°C$ | | | | | | |
| * Flux Density @ 1,194 A/m (15.0e) | B_m | G mT | 5,000 500 | 5,000 500 | 4,900 490 | 4,300 430 | 4,300 430 | 4,200 420 |
| * Remanence | B_r | G mT | 1,100 110 | 1,100 110 | 1,200 120 | 1,000 100 | 800 80 | 800 80 |
| * Coercivity | H_k | Oe A/m | 0.18 14 | 0.18 14 | 0.2 16 | 0.1 8 | 0.04 3 | 0.04 3 |
| Disaccommodation Factor | D_f | 10^{-6} | | | | <3 | <3 | <2.5 |
| * Resistivity | ρ | $\Omega \cdot m$ | 6 | 5 | 2 | 1 | 0.15 | 0.1 |
| * Density | δ | g/cm ³ | 4.8 | 4.8 | 4.8 | 4.8 | 4.8 | 4.9 |
| Power Loss (P_f) Sine Wave, In mW/cm ³ (typical) | 25kHz 200mT (2,000G) | @25°C @60°C @100°C @120°C | 130 85 70 85 | 120 90 95 130 | 90 160 240 | | | |
| | 100kHz 100mT (1,000G) | @25°C @60°C @100°C @120°C | 140 100 70 90 | 125 90 125 165 | 100 180 225 | | | |
| | 500kHz 50mT (500G) | @25°C @60°C @100°C @120°C | 375 300 250 300 | 300 250 275 350 | | | | |
| | 700kHz 50mT (500G) | @25°C @60°C @100°C @120°C | | | | | | |
| Available In: | Pol Cores | | X | X | X | X | X | |
| | RS Cores | | X | X | X | X | X | |
| | BS Cores | | X | X | X | X | X | |
| | RM Cores | | X | X | X | X | X | |
| | EP Cores | | X | X | X | X | X | |
| | E, U Cores | | X | X | X | X | X | |
| | EE, ETD Cores | | X | X | X | X | X | |
| | PQ Cores | | X | X | X | | | |
| | Toroids | | X | | | X | X | X |
| | Blocks | | | | | X | | |

Note: These characteristics are typical for a 42206 size (0.870" O.D.) toroid. Specific core data will usually differ from these numbers due to the influence of geometry and size. Characteristics with a * are typical.

P-material ferrite was chosen due to the availability of the product directly from the manufacturer. The size of the coupler was determined by calculating the WaAc/power output relationship [8] and using this result in a lookup table to determine the E-core required. The WaAc relationship is developed as follows:

$$E = 4BA_c N f \times 10^{-8} \text{ (Faraday's Law for a square wave)}$$

$$K = \frac{NA_w}{W_a} \quad \text{--->} \quad NA_c = \frac{KW_a A_c}{A_w}$$

$$C = \frac{A_w}{I}$$

$$e = \frac{P_o}{P_i}$$

$$P_i = EI$$

And therefore,

Equation 1

$$WaAc = \frac{P_o C * 10^8}{4eBfK} = 9.38cm^4$$

Where:

- E: applied voltage (RMS)
- A_c: core area in cm²
- N: number of turns
- A_w: wire area in cm²
- W_a: window area in cm² (of the bobbin)
- I: current (RMS)

- P_i: input power
- P_o: output power (Conservative: 800W)
- C: current capacity in cm²/amp (5.07 x 10⁻³ for E-core with square wave)
- e: efficiency (90% for transformer)
- B: flux density in gauss (conservative, 2kG for P-material (max is 5kG))
- f: frequency in Hz (20000)
- K: 0.30 for E cores (primary side only)

For a WaAc value of 9.38cm⁴, the recommended core is at least the size of either a 47035 or 47228. Again, the 47228 core was selected because of its immediate availability from the manufacturer.

The size of a magnetic component is directly related to the magnitude of acceptable losses. The losses can generally be broken into three main categories: i^2R , hysteresis, and eddy current. The inductive coupler is modeled using the model for a real transformer. The standard equivalent circuit for a transformer is shown in Figure 6 . The model is provided by the American National Standards Institute, in conjunction with the IEEE, in ANSI/IEEE Std 390-1987, "An American National Standard – IEEE Standard for Pulse Transformers" [1]. All of the components do not necessarily need to be included in the evaluation of the pulse transformer (i.e. the capacitive elements are typically negligible and can be ignored). Therefore, the equivalent circuit can be reduced to that shown in Figure 7.

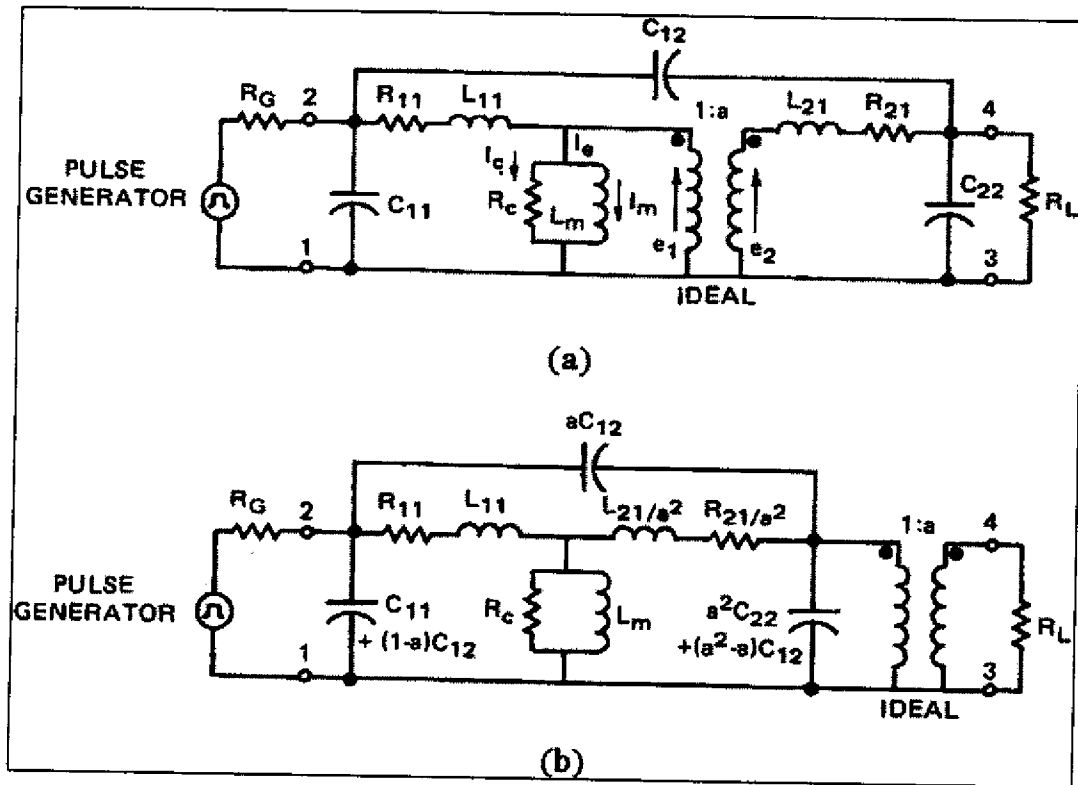


Figure 6: (a) Complete Equivalent Circuit for a Pulse Transformer (b) Alternate Form of Complete Equivalent Circuit for a Pulse Transformer [1]

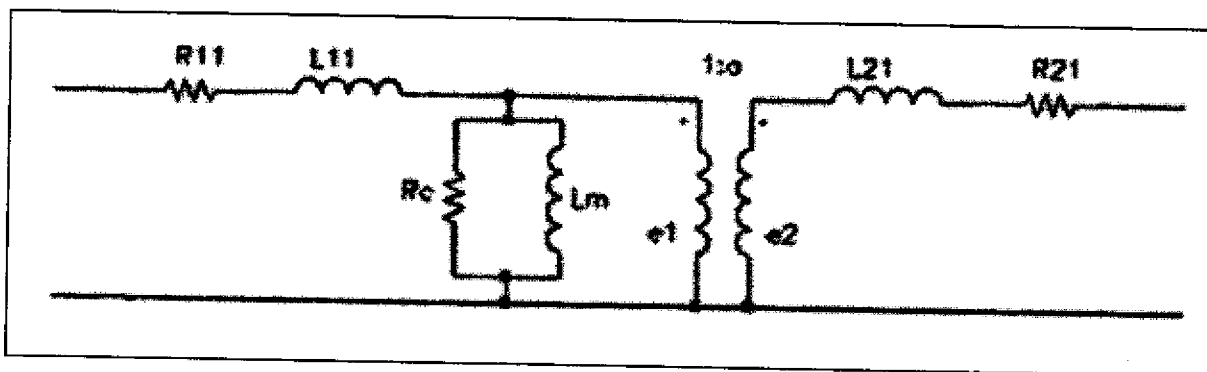


Figure 7: Simplified IEEE Equivalent Circuit [1]

Terms associated with Figure 6 and Figure 7:

| | |
|--------------------|---|
| a: | transformer ratio. Where the coefficient coupling is high, $a = N_2/N_1$ |
| C_{11}, C_{22} : | equivalent self capacitance, winding indicated by subscripts |
| C_{12} : | equivalent mutual capacitance between windings 1 and 2 |
| L_{11}, L_{22} : | self inductance of winding indicated by subscript |
| L_{11}, L_{21} : | leakage inductance of winding designated by first subscript |
| L_m : | magnetizing inductance |
| N_1 : | primary turns |
| N_2 : | secondary turns |
| R_{11}, R_{21} : | resistance associated with leakage inductance, referred to winding indicated by first subscript |
| R_c : | equivalent core-loss resistance, under pulse conditions shunt representation |

2.1.1 Magnetizing Inductance

Two windings are magnetically coupled by the flux density (B) that is created by one winding and linked to the other. The ideal condition is for the flux density (B) to be present without any magnetic field intensity (H). This is never the case because there is always some finite permeability in the core. The best case for achieving the ideal condition is to use a highly permeable core with no air gap. The Magnetizing Inductance (L_m) represents the inductance that results from the relationship between the two windings and the core geometry. For a simple inductor, the magnetizing inductance for a core with an air gap is:

Equation 2

$$L_m = \frac{\mu_0 AN^2}{(\mu_0/\mu_c)l_c + g}$$

Where:

- μ_0 : permeability of air
- μ_c : permeability of core
- A: core/gap area
- l_c : effective length of the core
- N: turns
- g: gap length

The value of the magnetizing inductance becomes independent of the core's magnetic properties if:

Equation 3

$$g \gg \frac{\mu_0 l_c}{\mu_c}$$

The gap is routinely introduced to make the inductance value predictable and stable, even with changes to the properties of the magnetic material due to temperature, flux level, sample and manufacturer [5][pg 573]. Therefore, the inductive coupler has a magnetizing inductance of:

Equation 4

$$L_{mag} = \frac{\mu_0 A_c N_1^2}{g}$$

The disadvantage with increasing the gap too much is that the magnetizing inductance decreases, correspondingly, and the transformer becomes farther from ideal. The result is that

the magnetizing current will increase proportionately due to the decrease in the magnetizing reactance by:

Equation 5

$$X_m = j\omega L_m$$

In the case of the inductive coupler, this means that the gap must be large enough to provide stability and small enough to minimize its effects on the magnetizing current.

Additional anomalies that affect the magnetizing inductance are fringing fields and non-uniform flux density. Fringing fields occur at the gap and are caused by the flux leaving the high permeability of the core and entering the low permeability of the air. Most of the flux is trapped on the other side of the air gap, but some escapes and results in an increase in the effective cross-sectional area of the gap. This in turn results in an increase from the expected magnetizing inductance. Non-uniform flux density is a result of the difference in potential at different parts of the core; say the inner and outer surface. The effect is that the portion with the higher flux density may increase in temperature and ultimately result in “hot spots.” [10]

2.1.2 Leakage Inductance

“Not all the magnetic flux created by one winding of a two-winding transformer follows the magnetic path and links the other winding; some of the flux “leaks” from the core and returns through the air. The result is that each winding links some of the flux that is not linked by the other, causing imperfect coupling [5] [pg 590].” The result is that not all the voltage from the primary is transformed to the secondary.

The leakage inductance can be calculated by first determining the total stored magnetic energy in these fields by:

Equation 6 [10]

$$U_m = \int_v \frac{1}{2} \mu_0 H^2 \partial v = \frac{1}{2} L_{eq} i^2$$

Once the stored magnetic energy is known, the equivalent inductance can be determined.

The leakage inductance can be reduced by one of three methods. First, because the leakage inductance is proportional to the volume of the interwinding spaces, simply reduce the distance between conductors. This can be accomplished by using litz wire, described later. Second, increase the width of the transformer windings. Lastly, split either the primary or the secondary windings in half and use them to surround the other windings. Splitting the windings has the greatest impact on reducing the leakage inductance due to its quadratic nature [10].

2.1.3 Copper Losses

Generally, the copper loss is a straight forward calculation of length times the resistance per unit length. However, if the application operates at a higher frequency (>10 kHz), there is an additional anomaly called skin effect. Skin effect is caused by the fields created by the conductor's own current. Neither the electric nor magnetic fields penetrate far into a good conductor. Skin depth is a measure of the lateral penetration of current in a conductor. Skin depth is the point where the fields are reduced by a factor of 1/e (or 0.368). A general equation for skin depth is:

Equation 7

$$\delta = \sqrt{\frac{2}{\omega \mu \sigma}}$$

Where:

δ : skin depth

- ω : angular frequency of excitation ($2\pi \cdot f$)
- σ : conductivity of the material
- μ : permeability of the material

Skin effect can be minimized by the use of stranded wire, called litz, or foil.

2.1.4 Core Losses

Hysteresis and eddy currents cause additional core loss. Hysteresis is related to the enclosed area of the B-H profile of the core. It is the result of unrecoverable energy expended to rotate magnetic domains within a magnetic material. The energy lost per cycle per unit volume of material is:

Equation 8

$$E = \oint d\omega_m = \oint \vec{H} \cdot d\vec{B}$$

which is the area enclosed by the material's hysteresis loop. The total hysteresis loss is then a product of this area, the frequency, and the volume of the core.

Eddy current loss is simply the i^2R loss caused by currents induced in the magnetic material. These eddy currents are driven by a voltage induced in the material, by Faraday's Law, and as a result they flow in a plane perpendicular to the magnetic flux density (B) [5][pg583]. Resistivity of the core results in two effects, both effects are caused by the changing magnetic flux in the finite resistivity core which induces eddy currents, similar to the skin effect in the conductor. The first effect is power dissipation that is a function of the resistivity, frequency of excitation, and core geometry. This loss can be calculated by dividing the cross-section of the core into parallel resistive paths, determining the voltage induced in each and the resistance of the path, and calculating the power dissipation by:

Equation 9

$$P = \frac{v^2}{R}.$$

The second effect of eddy currents in the core is magnetic shielding. Shielding causes the magnetic flux to be attenuated toward the center of the core, like skin effect in conductors [10].

Magnetics provides a method for determining the core loss in their cores as:

Equation 10 [9]

$$P_L = af^c B^d$$

Where:

a, c, d: factors applied to the equation based on frequency of operation and material chosen (See Table 3: Core Loss Factors [9])

f: frequency in kHz

B: flux density in kG

Table 3: Core Loss Factors [9]

| | | | | |
|------------|--|-----------------------|------|------|
| R Material | $f < 100 \text{ kHz}$ | 0.074 | 1.43 | 2.85 |
| | $100 \text{ kHz} \leq f < 500 \text{ kHz}$ | 0.036 | 1.64 | 2.68 |
| | $f \geq 500 \text{ kHz}$ | 0.014 | 1.84 | 2.28 |
| P Material | $f < 100 \text{ kHz}$ | 0.158 | 1.36 | 2.86 |
| | $100 \text{ kHz} \leq f < 500 \text{ kHz}$ | 0.0434 | 1.63 | 2.62 |
| | $f \geq 500 \text{ kHz}$ | 7.36×10^{-7} | 3.47 | 2.54 |
| F Material | $f < 10 \text{ kHz}$ | 0.790 | 1.06 | 2.85 |
| | $10 \text{ kHz} \leq f < 100 \text{ kHz}$ | 0.0717 | 1.72 | 2.66 |
| | $100 \text{ kHz} \leq f < 500 \text{ kHz}$ | 0.0573 | 1.66 | 2.68 |
| | $f \geq 500 \text{ kHz}$ | 0.0126 | 1.88 | 2.29 |
| J Material | $f \leq 20 \text{ kHz}$ | 0.245 | 1.39 | 2.50 |
| | $f > 20 \text{ kHz}$ | 0.00458 | 2.42 | 2.50 |
| W Material | $f \leq 20 \text{ kHz}$ | 0.300 | 1.26 | 2.60 |
| | $f > 20 \text{ kHz}$ | 0.00382 | 2.32 | 2.62 |
| H Material | $f \leq 20 \text{ kHz}$ | 0.148 | 1.50 | 2.25 |
| | $f > 20 \text{ kHz}$ | 0.135 | 1.62 | 2.15 |

2.2 Power Electronics

2.2.1 AC to AC Converter

The purpose of the AC to AC Converter is to convert the 120VAC, 60Hz input power to a higher frequency output. The higher frequency is required to keep the size of the components of the inductive coupler at a more reasonable value. The conversion is completed in two steps: an AC to DC conversion and a DC to AC conversion.

The AC to DC conversion can be done by simply connecting the 120VAC line input to a full-wave bridge rectifier, as shown in Figure 8. The input waveform is shown in Figure 9. The waveform shown in Figure 9 represents the peak value of 169VAC and the RMS value of 120VAC. Figure 10 adds the waveform of the output of the rectifier.

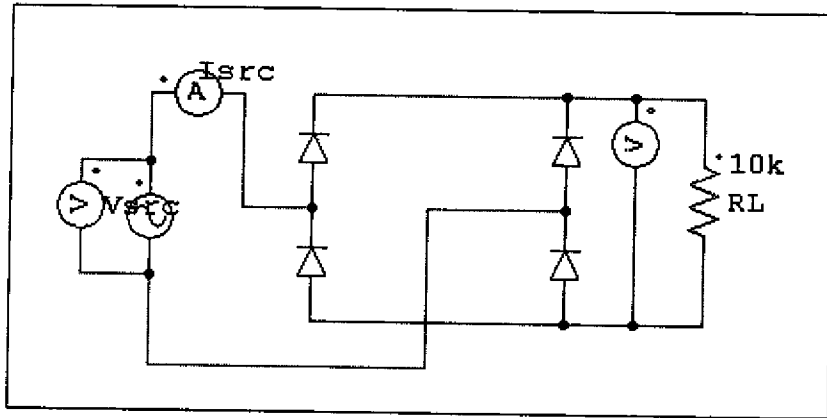


Figure 8: Full-Wave Bridge Rectifier

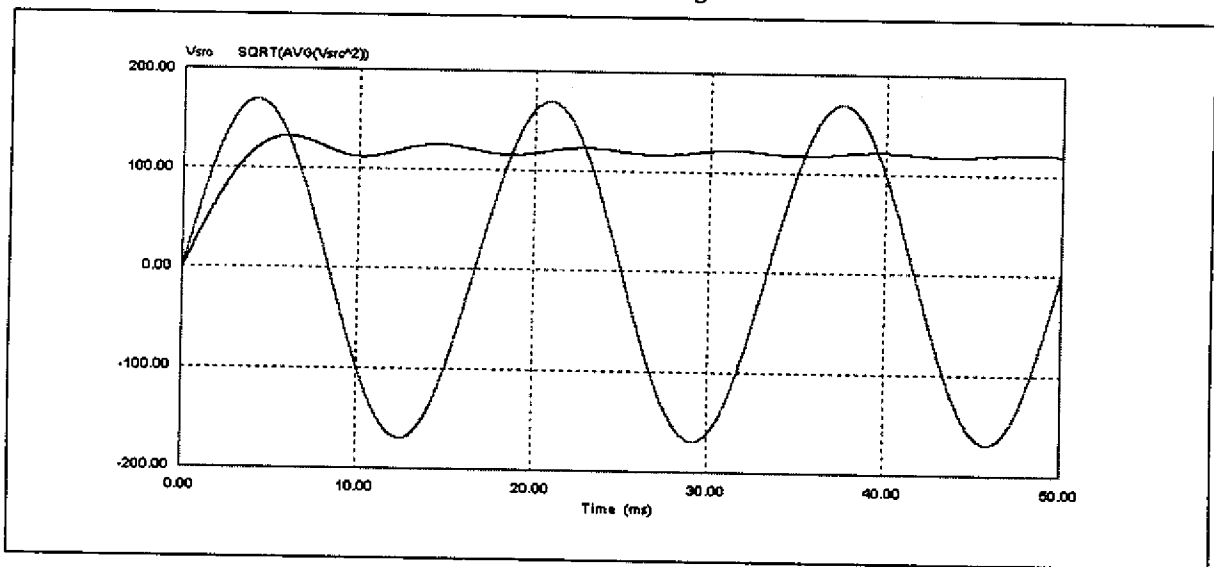


Figure 9: Input Waveform (Full-Wave Bridge Rectifier)

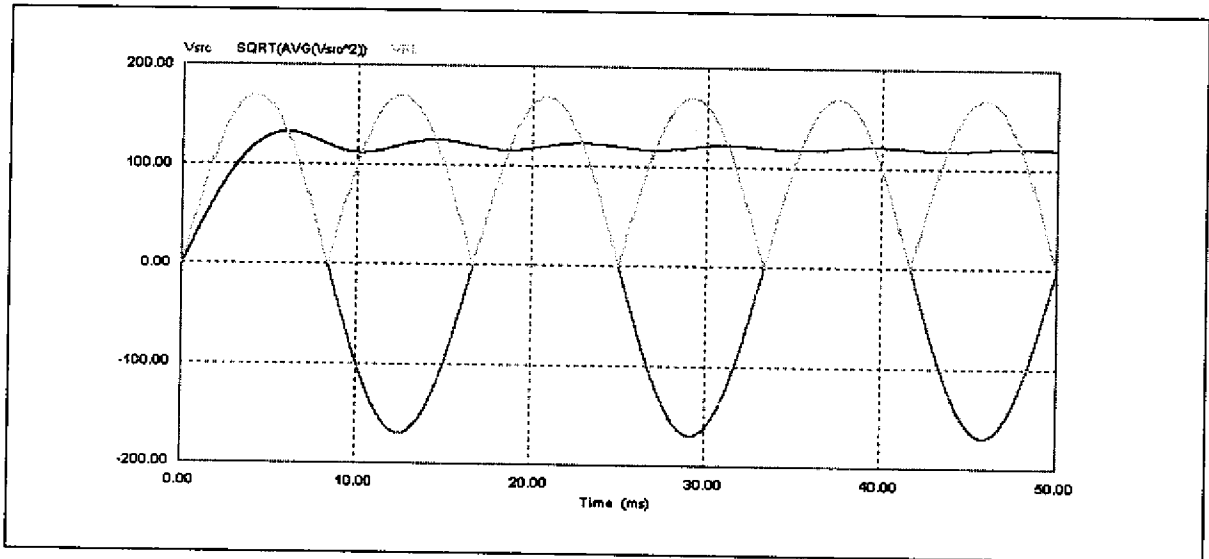


Figure 10: Output Waveform Added to Figure 9

A capacitor is added in parallel to the output of the rectifier to smooth the ripple voltage. The larger the size of the capacitor used the smoother the voltage output waveform. The value of the capacitor shown in Figure 11 is set to allow the reader to see the altered waveform, shown in Figure 12. In practice, the size of the capacitor should be large enough to minimize the ripple to the desired level, but small enough to keep the “in-rush” current as small as practical. “In-rush” current is an issue at startup of the system due to the initial uncharged state of the capacitor. This can be explained by:

Equation 11

$$i_c = C \frac{dv_c}{dt}$$

For example, if $C = 2\mu\text{F}$, $dv_c = 169\text{V}$ and $dt = 1/120\text{Hz} = 8.3 \text{ msec}$, then the in-rush current is 41mA. But if the capacitor value is $2000 \mu\text{F}$, then the in-rush current will also go up by a factor of 1000 to 41A. This is significant and can lead to problems with tripping of in-line fuses and breakers. This will be discussed further in Chapter 3.

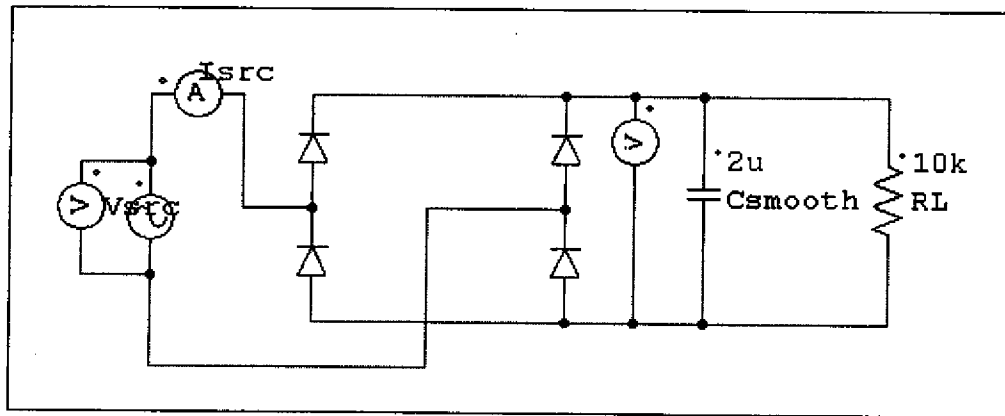


Figure 11: Smoothing Capacitor Added to Figure 8

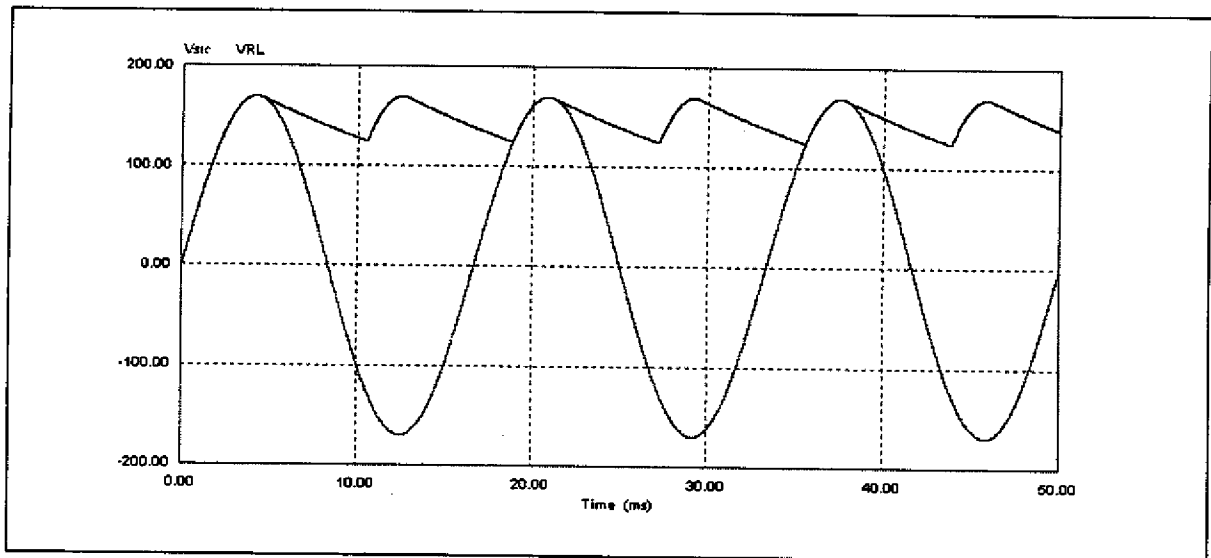


Figure 12: Input/Output Waveform with Added Smoothing Capacitor

The conversion from DC to AC is a little more difficult. There are many ways to make this conversion, but only two will be considered here. The two methods described are the half-bridge and the full-bridge (typically referred to as H-bridge). The switching frequency described below is set to 500Hz for a better view of the waveforms. However, the actual frequency used will be much higher; on the order of 20 kHz.

The half-bridge uses a combination of two switches (MOSFETs) and a snubber capacitor for each leg. The half- bridge circuit is shown in Figure 13. The capacitors act to maintain a fairly constant voltage across the switches. The gate switch is used for simulation purposes. It performs the function of turning the gate of the MOSFET on and off based on the switching frequency (500Hz). The top switch turns on at 1° and off at 179° (corresponding to 6 μsec and 994 μsec, respectively). The bottom switch operates on the other half cycle (181° - on and 359° - off). This turns the MOSFETs on sequentially and creates a 500Hz output. There is a delay time that is purposefully present to prevent both the switches from being on at the same time, creating a direct short circuit. The downfall to this circuit is the lower output voltage (see Figure 14). This is because the output is taken off the bottom switch/capacitor pair. In the case of the inductive coupler, the voltage needs to be maintained as high as possible to keep the current at a reasonable value. Keeping the current at a reasonable value minimizes the conductor size and allows for more turns on the coupler. For this reason, the half-bridge is not the best choice.

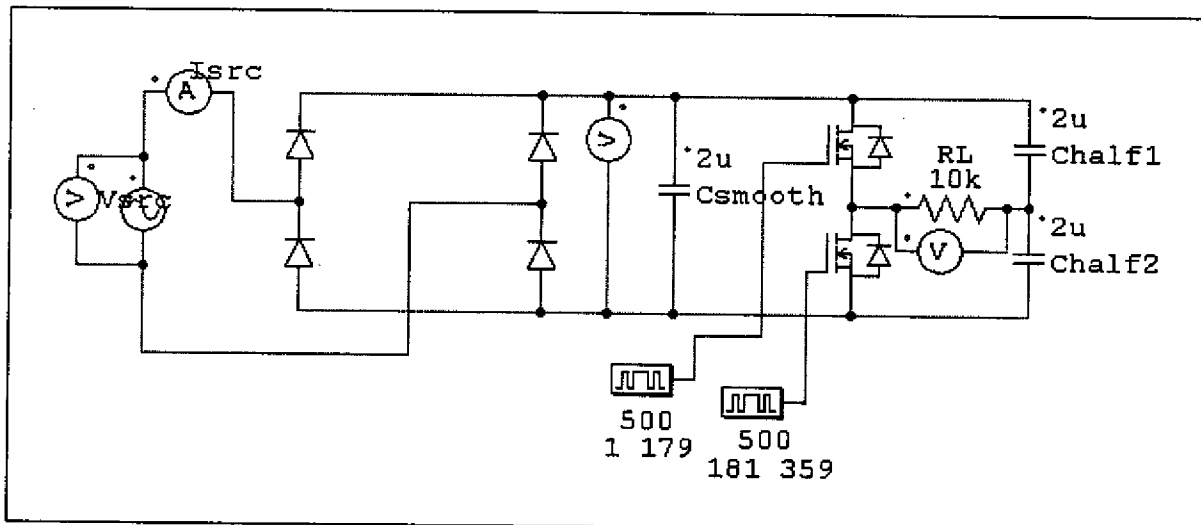


Figure 13: Half-bridge Circuit Diagram

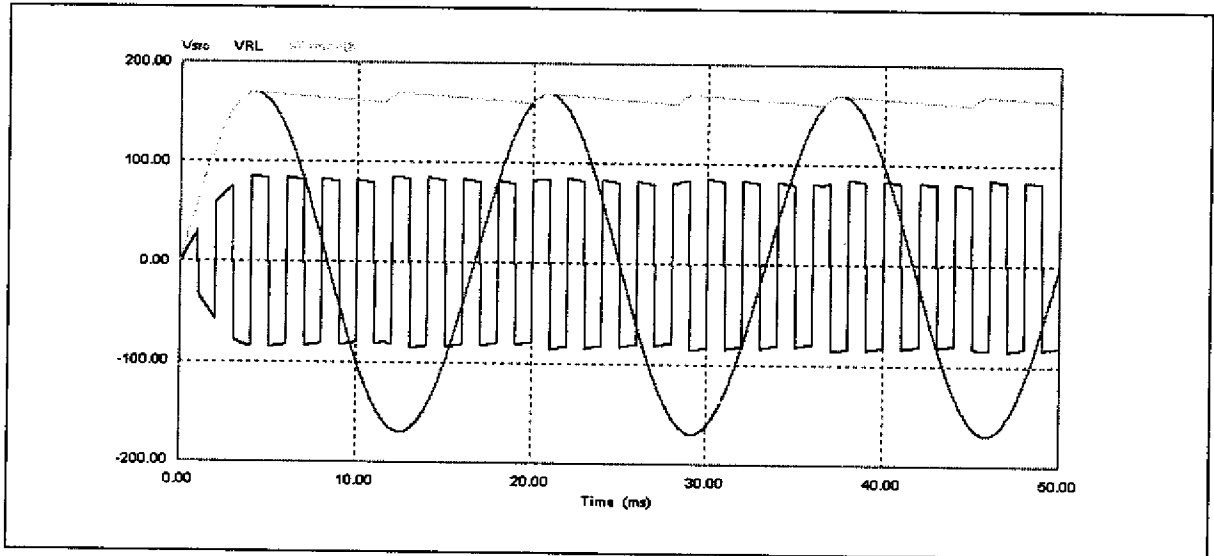


Figure 14: Half-bridge Waveforms

The H-bridge is similar in construction to the half-bridge, except it uses four switches rather than a switch/capacitor pair. The timing of the circuit is a little more complicated than the half-bridge only because the gate switch must be sent to offsetting switches, such as the top right and bottom left in Figure 15. The advantage is that the output voltage follows the smoothed capacitor voltage. The output voltage is shown in Figure 16 (with the other comparative voltage waveforms) and Figure 17 (stand-alone).

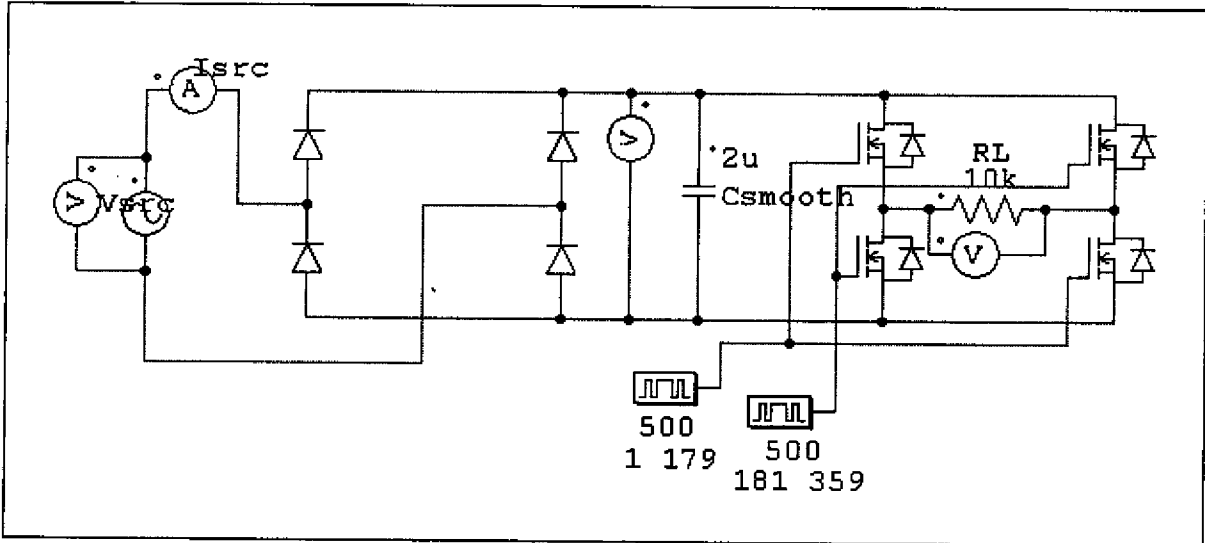


Figure 15: Full-bridge (H-bridge) Circuit Diagram

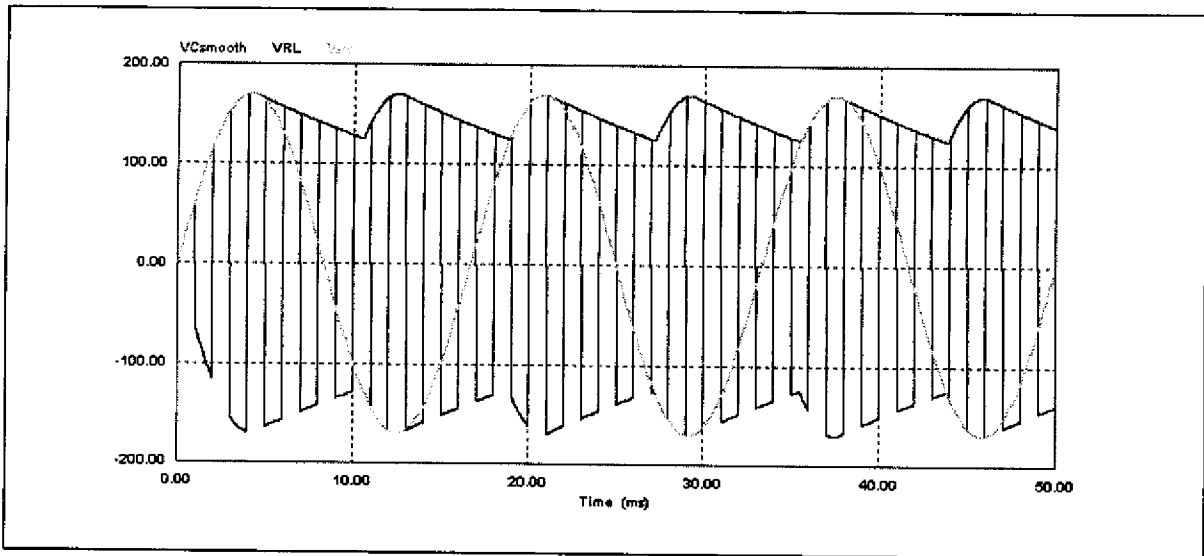


Figure 16: Full-bridge Waveforms

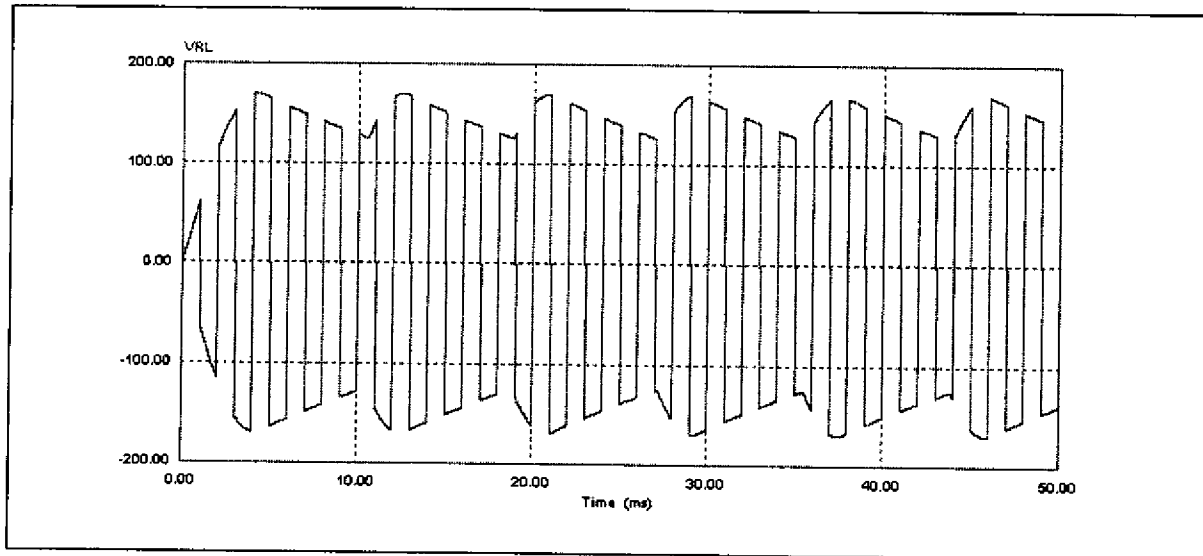


Figure 17: Full-bridge Output Waveform

2.2.2 AC to DC Converter

The purpose of the AC to DC converter is to convert the high frequency output of the inductive coupler to DC to charge the battery. This is completed in two stages: a full-bridge rectifier and a DC to DC converter. The full-bridge rectifier is similar to the one in section 2.2.1 and will not be discussed further. A DC to DC converter is used to reduce (“Buck”) or increase (“Boost”) the output voltage from the input voltage. Because the system is being designed to have a higher input than output voltage, only a “Buck” converter will be discussed.

The following describes how the “Buck” converter operates and refers to the circuit of Figure 18. It is initially assumed that C_{in} and L_{buck} are large enough that the resulting small values of external input network impedance and output network conductance will result in acceptably small ripples in all terminal variables. Because the inductor can not support an average voltage drop, $V_o = D \cdot V_{DC}$ (where D is the duty ratio of the series switch). Therefore, the duty ratio is defined as:

Equation 12

$$D = \frac{V_o}{V_{DC}}$$

Similarly, the capacitor can not carry an average current and thus $I_{in} = D \cdot I_{lbuck}$. The freewheeling diode, D_{free} , is switched on and off by the operation of the series switch (a MOSFET, in this case). When the switch is shut V_{DC} reverse biases the freewheeling diode, turning it off. When the switch opens, the continuity of current in L_{buck} forces the diode to conduct [5].

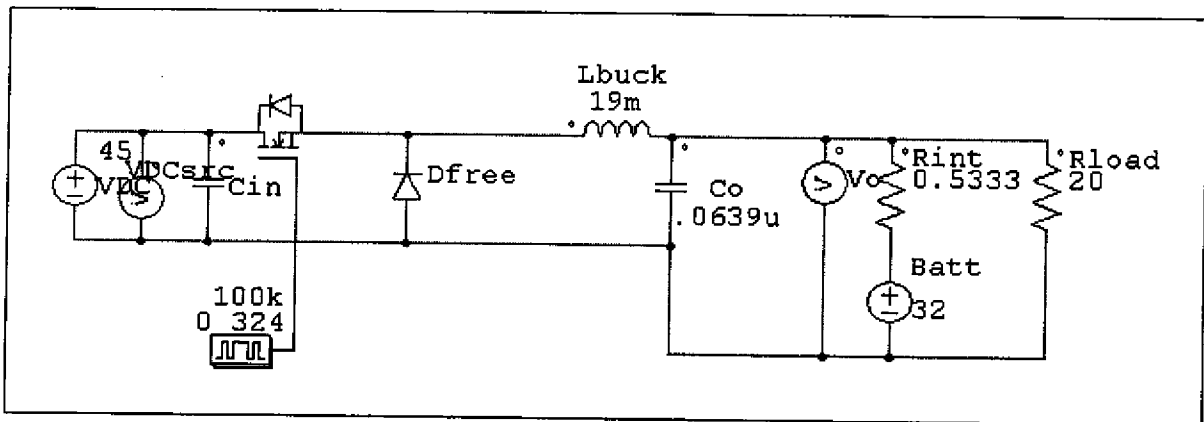


Figure 18: DC to DC (Buck) Converter

In order to maintain the converter in CCM (continuous conduction mode), there are limitations on the size of the passive elements. Specifically, the value of L_{buck}/R_{load} must be much greater than the period T ($1/f$) of the switching frequency. The minimum value of L_{buck} to satisfy this requirement is:

Equation 13

$$L_{min} = \frac{V_{ow}^2(1-D)T}{2P_{min}}$$

In the proposed case, P_{min} will occur when the battery charge is complete. At that time the only power being supplied is for normal loads (2A).

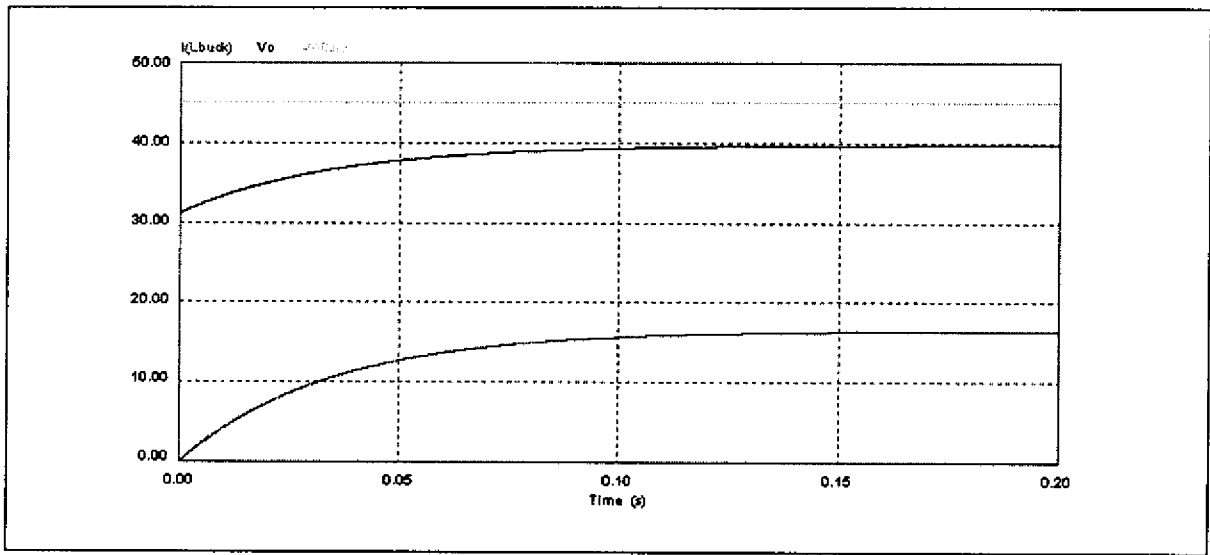


Figure 19: Buck Converter Waveforms

Chapter 3 Modeling and Simulation

Simulation and modeling of the system was completed by using the theory described in Chapter 2. Specific information is provided to help the understanding of the entire system concept.

3.1 Inductive Coupler

A MATLAB code was written to vary the number of primary turns and compare the core loss with the primary winding loss to minimize the overall losses in the system as discussed in 2.1. The primary voltage was assumed to be 155V to account for losses in the circuitry on the input to the inductive coupler. These losses include the voltage drop associated with the full-bridge rectifier, nominally 0.7V for each diode, and I^2R losses in the conductors. A graph of the losses versus the number of turns is shown in Figure 20 with actual numbers in Table 4.

As can be seen from the graph and table (highlighted), the total losses are minimized with 20 primary turns. 8 secondary turns are used in order to achieve the appropriate turns-ratio to transform the secondary voltage down to 60V. The secondary windings are split into 2 sections to surround the primary windings and minimize the leakage inductance. 36AWG litz magnet wire was used for both the primary and secondary windings. The conductor is small enough to minimize the skin effects in the windings as proven in the columns “RpDC” and “RpAC.” Columns “Spri” and “Ssec” are the number of actual strands of 36AWG wire required to carry the load current. Columns “BobInnPri” and “BobInnSec” are the inner bobbin widths required to hold the total primary turns and half of the secondary turns (due to being split). “Leakp” was calculated based on Equation 6, assuming that half of the equivalent inductance was due to the

primary. The other half of the equivalent inductance was then transformed across to determine “Leaks.”

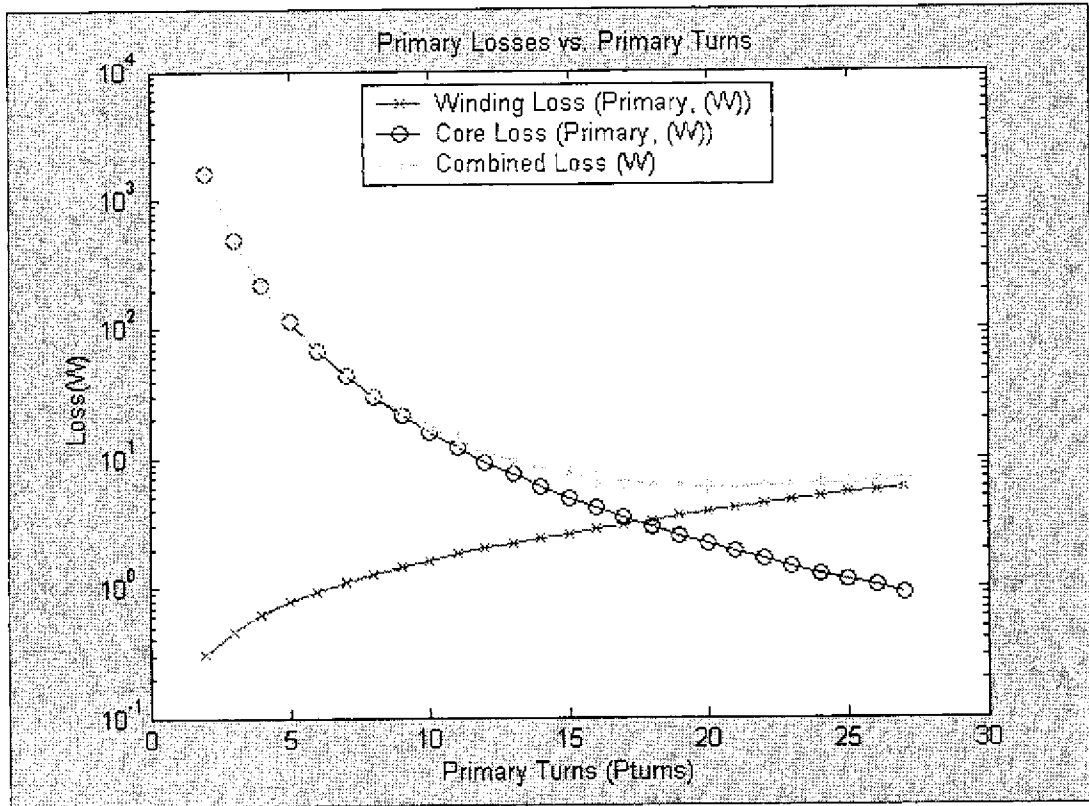


Figure 20: Primary Losses vs. Primary Turns

Table 4: Core Parameters vs. Primary Turns

| Table of Parameters with Gap Length = 0.50mm and AWG = 36, C = 250A/cm ² , Vpri=155, Vsec=60 | | | | | | | | | | | | | | | | | |
|---|--------|--------|------|---------|---------|----|-------|-----|--------|--------|---------|----------|-------|-------|-----------|-----------|---------|
| Np | Lm | Lleakp | Spri | RpDC | RpAC | Ns | LeakS | Ss | RsDC | RsAC | Pc | Rc | Wp | Wside | BobinnPri | BobinnSec | Losses |
| | uH | uH | | mohm | mohm | | uH | | mohm | mohm | W | Ohm | mm | mm | mm | mm | W |
| 2.0 | 3.70 | 0.09 | 174 | 15.108 | 15.131 | 2 | 0.09 | 449 | 5.855 | 5.864 | 1573.80 | 15.27 | 10.78 | 12.55 | 6.08 | 7.85 | 1574.91 |
| 3.0 | 8.32 | 0.21 | 174 | 22.663 | 22.748 | 2 | 0.09 | 449 | 5.855 | 5.864 | 493.55 | 48.68 | 12.70 | 11.58 | 8.00 | 6.89 | 494.81 |
| 4.0 | 14.80 | 0.41 | 174 | 30.217 | 30.439 | 2 | 0.10 | 449 | 5.855 | 5.864 | 216.77 | 110.83 | 14.21 | 10.83 | 9.51 | 6.13 | 218.19 |
| 5.0 | 23.12 | 0.69 | 174 | 37.771 | 38.232 | 2 | 0.11 | 449 | 5.855 | 5.864 | 114.51 | 209.81 | 15.41 | 10.23 | 10.72 | 5.53 | 116.09 |
| 6.0 | 33.30 | 1.55 | 174 | 45.325 | 46.159 | 4 | 0.69 | 449 | 11.710 | 11.796 | 67.98 | 353.41 | 12.70 | 11.58 | 8.00 | 6.89 | 70.53 |
| 7.0 | 45.32 | 2.21 | 174 | 52.880 | 54.247 | 4 | 0.72 | 449 | 11.710 | 11.796 | 43.74 | 549.22 | 13.50 | 11.19 | 8.80 | 6.49 | 46.46 |
| 8.0 | 59.19 | 3.02 | 174 | 60.434 | 62.527 | 4 | 0.76 | 449 | 11.710 | 11.796 | 29.86 | 804.65 | 14.21 | 10.83 | 9.51 | 6.13 | 32.74 |
| 9.0 | 74.92 | 3.98 | 174 | 67.988 | 71.027 | 4 | 0.79 | 449 | 11.710 | 11.796 | 21.32 | 1126.94 | 14.84 | 10.51 | 10.14 | 5.82 | 24.37 |
| 10.0 | 92.49 | 5.09 | 174 | 75.542 | 79.778 | 4 | 0.81 | 449 | 11.710 | 11.796 | 15.77 | 1523.24 | 15.41 | 10.23 | 10.72 | 5.53 | 19.01 |
| 11.0 | 111.91 | 7.68 | 174 | 83.096 | 88.809 | 6 | 2.29 | 449 | 17.565 | 17.888 | 12.01 | 2000.55 | 13.74 | 11.06 | 9.04 | 6.37 | 16.26 |
| 12.0 | 133.18 | 9.37 | 174 | 90.651 | 98.149 | 6 | 2.34 | 449 | 17.565 | 17.888 | 9.36 | 2565.82 | 14.21 | 10.83 | 9.51 | 6.13 | 13.80 |
| 13.0 | 156.31 | 11.24 | 174 | 98.205 | 107.828 | 6 | 2.39 | 449 | 17.565 | 17.888 | 7.45 | 3225.86 | 14.64 | 10.62 | 9.94 | 5.92 | 12.08 |
| 14.0 | 181.28 | 13.30 | 174 | 105.759 | 117.875 | 6 | 2.44 | 449 | 17.565 | 17.888 | 6.03 | 3987.43 | 15.04 | 10.42 | 10.34 | 5.72 | 10.86 |
| 15.0 | 208.10 | 15.55 | 174 | 113.313 | 128.319 | 6 | 2.49 | 449 | 17.565 | 17.888 | 4.95 | 4857.22 | 15.41 | 10.23 | 10.72 | 5.53 | 10.00 |
| 16.0 | 236.77 | 20.03 | 174 | 120.867 | 139.191 | 8 | 5.01 | 449 | 23.420 | 24.231 | 4.11 | 5841.85 | 14.21 | 10.83 | 9.51 | 6.13 | 10.25 |
| 17.0 | 267.29 | 22.90 | 174 | 128.422 | 150.519 | 8 | 5.07 | 449 | 23.420 | 24.231 | 3.46 | 6947.86 | 14.53 | 10.67 | 9.83 | 5.97 | 9.83 |
| 18.0 | 299.66 | 25.97 | 174 | 135.976 | 162.333 | 8 | 5.13 | 449 | 23.420 | 24.231 | 2.94 | 8181.75 | 14.84 | 10.51 | 10.14 | 5.82 | 9.55 |
| 19.0 | 333.88 | 29.24 | 174 | 143.530 | 174.662 | 8 | 5.18 | 449 | 23.420 | 24.231 | 2.52 | 9549.98 | 15.13 | 10.37 | 10.44 | 5.67 | 9.38 |
| 20.0 | 369.95 | 32.70 | 174 | 151.084 | 187.536 | 8 | 5.23 | 449 | 23.420 | 24.231 | 2.17 | 11058.92 | 15.41 | 10.23 | 10.72 | 5.53 | 9.30 |
| 21.0 | 407.87 | 38.73 | 174 | 158.639 | 200.985 | 10 | 8.78 | 449 | 29.275 | 30.916 | 1.89 | 12714.94 | 14.47 | 10.70 | 9.77 | 6.00 | 10.20 |
| 22.0 | 447.64 | 42.76 | 174 | 166.193 | 215.037 | 10 | 8.83 | 449 | 29.275 | 30.916 | 1.65 | 14524.32 | 14.72 | 10.58 | 10.02 | 5.88 | 10.25 |
| 23.0 | 489.26 | 46.96 | 174 | 173.747 | 229.723 | 10 | 8.88 | 449 | 29.275 | 30.916 | 1.46 | 16493.34 | 14.96 | 10.45 | 10.26 | 5.76 | 10.35 |
| 24.0 | 532.73 | 51.35 | 174 | 181.301 | 245.071 | 10 | 8.92 | 449 | 29.275 | 30.916 | 1.29 | 18628.21 | 15.19 | 10.34 | 10.49 | 5.64 | 10.50 |
| 25.0 | 578.05 | 55.92 | 174 | 188.855 | 261.111 | 10 | 8.95 | 449 | 29.275 | 30.916 | 1.15 | 20935.12 | 15.41 | 10.23 | 10.72 | 5.53 | 10.68 |
| 26.0 | 625.22 | 62.70 | 174 | 196.410 | 277.873 | 12 | 13.36 | 449 | 35.130 | 38.036 | 1.03 | 23420.21 | 14.64 | 10.62 | 9.94 | 5.92 | 11.87 |
| 27.0 | 674.24 | 67.67 | 174 | 203.964 | 295.386 | 12 | 13.37 | 449 | 35.130 | 38.036 | 0.92 | 26089.60 | 14.84 | 10.51 | 10.14 | 5.82 | 12.12 |

The inductive coupler was custom built using the 47228 ferrite core from Magnetics.

The gap was cut to a length of 0.5 mm using ceramic machining techniques. A cross-sectional view of the entire coupler is shown in Figure 21 and the respective dimensions in Figure 22. As can be seen from Figure 21, there is a small gap on each side of the primary “puck.” This allows enough room for the primary and secondary to have a thin coat of epoxy added for protection while leaving room for the “puck” to be inserted and removed from the secondary easily. Photos of the actual inductive coupler are shown in Figure(s) 23 through 27.

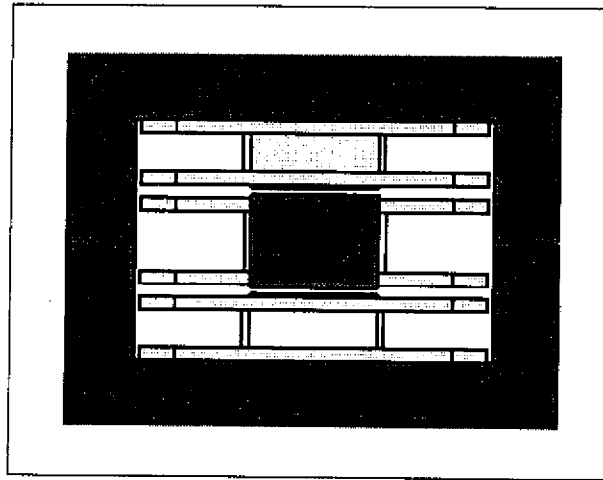


Figure 21: Inductive Coupler Cross-section (Shown with Primary Core Exposed)

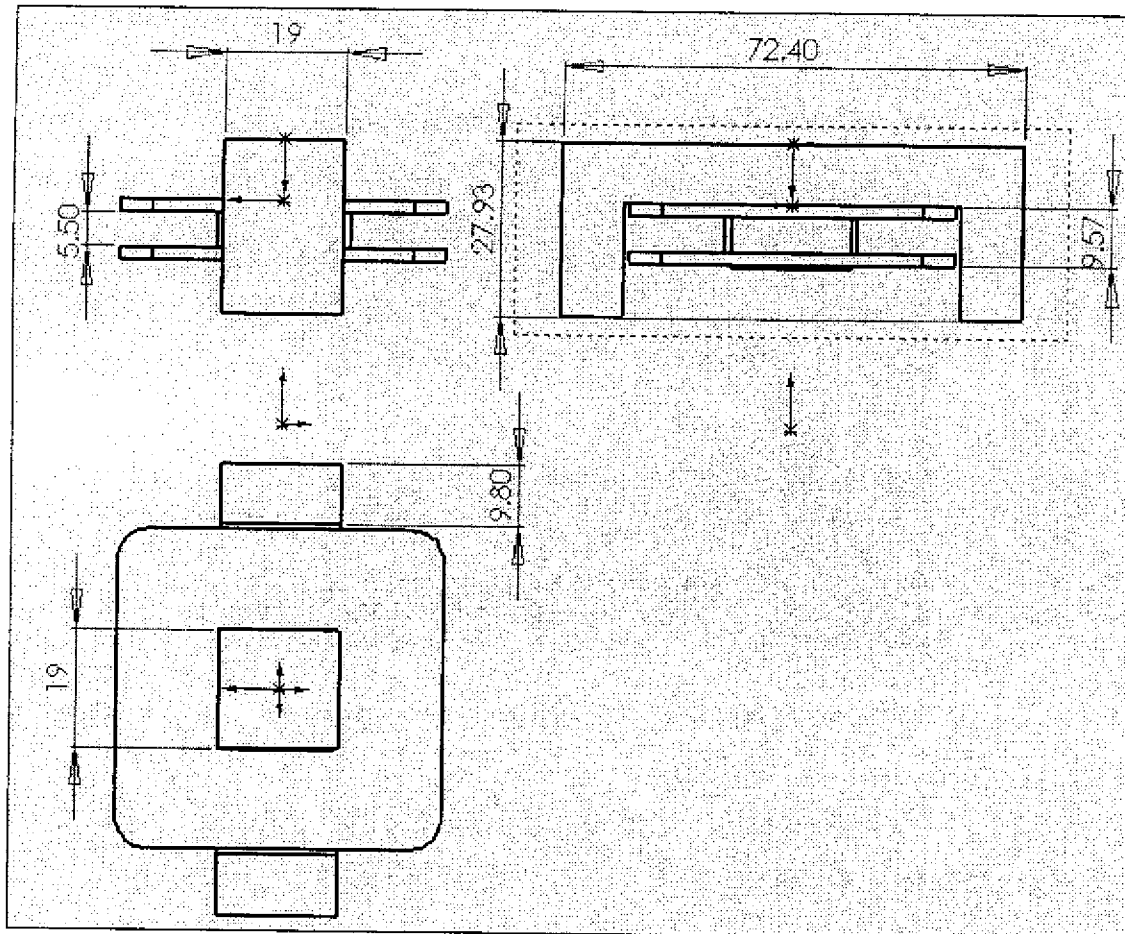


Figure 22: Inductive Coupler (One-half of Secondary) Dimensions (Shown in mm)

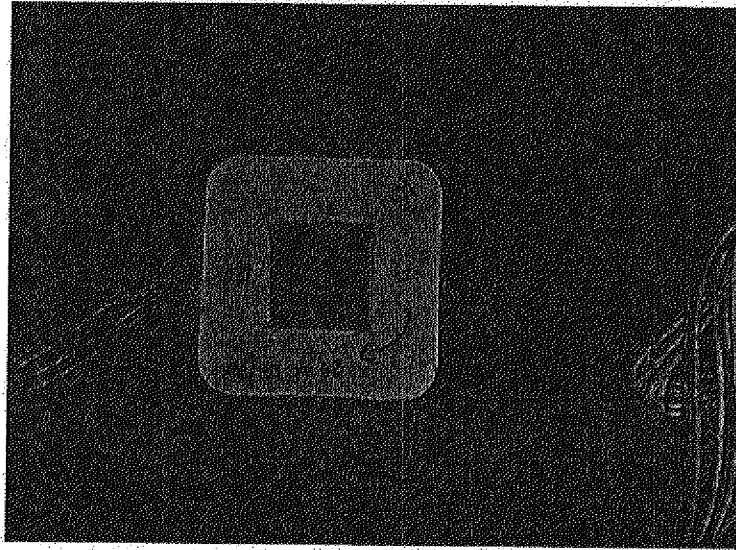


Figure 23: Top View of Primary ("Puck")



Figure 24: Side View of Secondary (Note Split Windings)

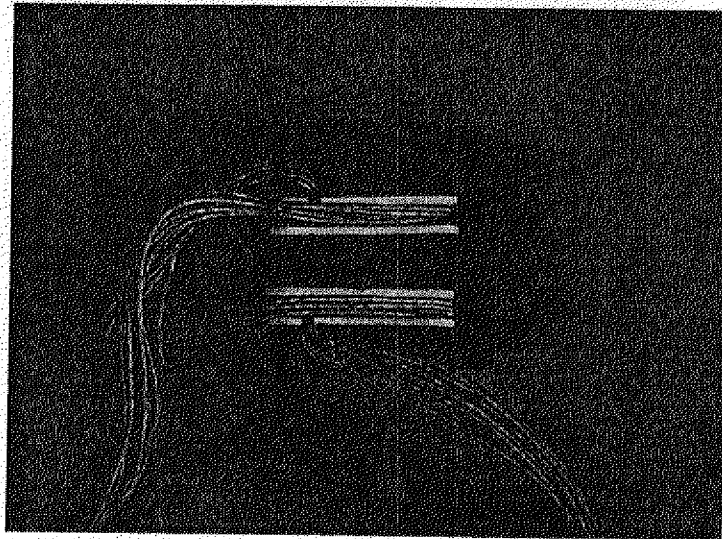


Figure 25: Back View of Secondary (Note Split Windings)

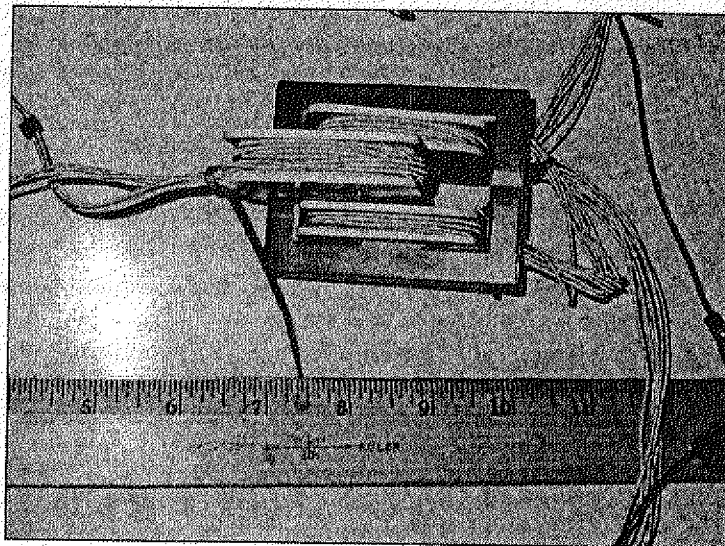


Figure 26: Front View with Primary Being Inserted

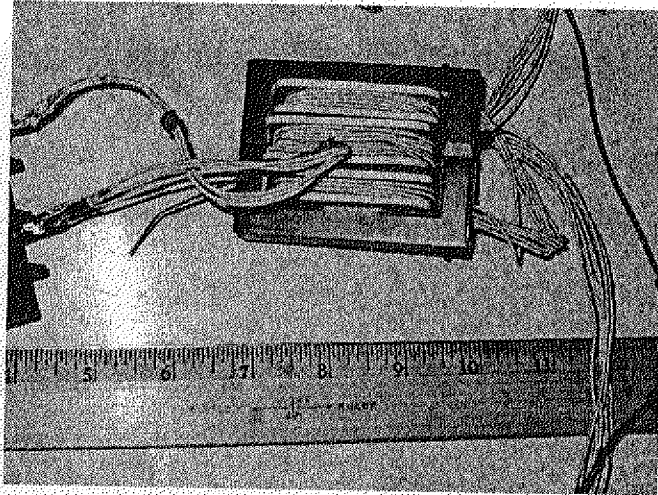


Figure 27: Front View with Primary Inserted

Once the inductive coupler was built, core parameters were measured using the HP 4192A LF Impedance Analyzer. This analysis was conducted at 20 kHz. The first measurement was taken from the primary leads with the secondary leads open-circuited, as shown in Figure 28. This measurement is used to determine the magnetizing inductance of the coupler. The second measurement was taken from the primary leads with the secondary short-circuited. This is used to determine the leakage inductance of the coupler. The third and fourth measurements were taken with only the primary or secondary core and respective windings. This is the winding resistance of the respective winding. The actual results are listed below in Table 5.

The next step is to use the measured parameters to determine the actual values of the inductive coupler (See Figure 28 and Figure 29), as follows:

Table 5: Inductive Coupler HP 4192A LF Impedance Analyzer Results

| | L | R |
|---|---------------|---------------|
| Entire Coupler with Secondary Open-Circuit | 300 μ H | 60 m Ω |
| Entire Coupler with Secondary Short-Circuit | 16.32 μ H | 92 m Ω |
| Primary Only, Windings and Core | 20.73 μ H | 23 m Ω |
| Secondary Only, Windings and Core | 5.79 μ H | 11 m Ω |

$$R_{ws}' = \frac{R_{ws}}{m^2} = \frac{11m\Omega}{(0.4)^2} = 69m\Omega \quad \text{Where m is the turns-ratio } 8/20$$

$$R_{wp} = 23m\Omega$$

$$R_{short} = R_{wp} + R_{ws}' = 23m\Omega + 69m\Omega = 92m\Omega$$

$$L_{short} = L_{leakp} + L_{leaks}' = 2L_{leakp} = 16.32\mu H$$

$$\text{Assuming: } L_{leakp} = L_{leaks}' = 8.16\mu H$$

$$L_{leaks} = L_{leaks}' m^2 = 1.31\mu H$$

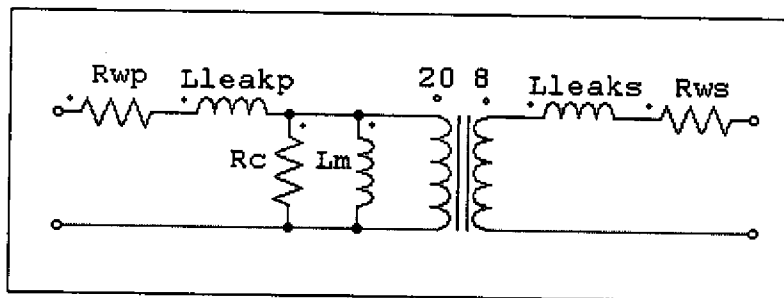


Figure 28: Inductive Coupler Parameters (Similar to Figure 7), Shown in Open Circuit

$$Z_{in} = R_{w_p} + j\omega L_{leak_p} + \frac{R_c j\omega L_m}{R_c + j\omega L_m} = 60m\Omega + j\omega 300\mu H$$

$$\frac{R_c j\omega L_m}{R_c + j\omega L_m} = 37m\Omega + j36.66\Omega$$

$$\frac{jR_c^2 \omega L_m + R_c (\omega L_m)^2}{R_c^2 + (\omega L_m)^2} = 37m\Omega + j36.66\Omega$$

Equation 14

$$\frac{R_c^2 \omega L_m}{R_c^2 + (\omega L_m)^2} = 36.66\Omega$$

Equation 15

$$\frac{R_c (\omega L_m)^2}{R_c^2 + (\omega L_m)^2} = 37m\Omega$$

Dividing Equation 14 by Equation 15 and solving for R_c

Equation 16

$$R_c = \frac{36.66\Omega}{37m\Omega} \omega L_m$$

Substituting Equation 16 into Equation 14 and solving for L_m and subsequently R_c

$L_m = 292\mu H$ and $R_c = 36.3 k\Omega$.

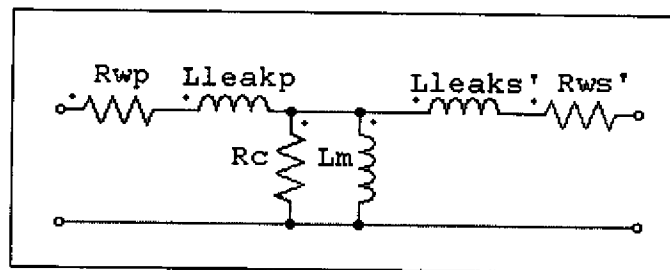


Figure 29: Inductive Coupler Parameters with Secondary Components Transformed

Table 6: Inductive Coupler Characteristics

| Parameter | Theoretical | Actual |
|-------------------------------|--------------------|-----------------|
| R_{wp} | 151 m Ω | 23 m Ω |
| L_{leakp} | 32.7 μ H | 8.16 μ H |
| R_C | 11.1 k Ω | 36.3 k Ω |
| L_m | 370 μ H | 292 μ H |
| R_{ws} | 23.4 m Ω | 11 m Ω |
| L_{leaks} | 5.23 μ H | 1.31 μ H |

Although the actual characteristics are of the same order of magnitude as the theoretical, it is worth noting the difference between the two magnetizing inductances. The theoretical magnetizing inductance is based on a gap of 0.5 mm. However, the actual magnetizing inductance corresponds to a gap length of 0.63 mm which is not unreasonable

3.2 Circuit Simulation

Once the actual core parameters were determined, simulation was performed using PSIM 6.0. The simulation circuit can be seen in Figure 30, and the resulting waveforms in Figure 31 and Figure 32.

The following is a discussion of specific portions of the circuit not discussed in Chapter 2 and refers to Figure 30. The passive components on the input to the full-bridge rectifier (BD11) are an RFI filter contained in the Corcom P Series power entry module. In addition, this module contains an in-line fuse for over current protection. The resistor matrix between the output of BD11 and the smoothing capacitor, $C=4400\mu$ F, is used to simulate how a thermistor would operate. A thermistor (CL-30) is required due to the high in-rush current the initially charge the

capacitor. A thermistor has a negative temperature gradient (i.e. as current flows and it the temperature increases, the resistance decreases) with a higher resistance at startup. MOS1 through 4 are MOSFETs used to convert the DC to AC. Attached to each gate is a timing block used to turn the MOSFET on and off based on the desired switching frequency. C_b is a blocking capacitor which blocks any DC bias from saturating the coupler. It is sized large enough to minimize the AC impedance at 20 kHz. MOS5, L1, D_{free} and the input and output capacitors make-up the “buck” converter. R_{int} represents the internal resistance of the battery. R_{load} represents the normal loading of 2A and assumes an output voltage of 40VDC.

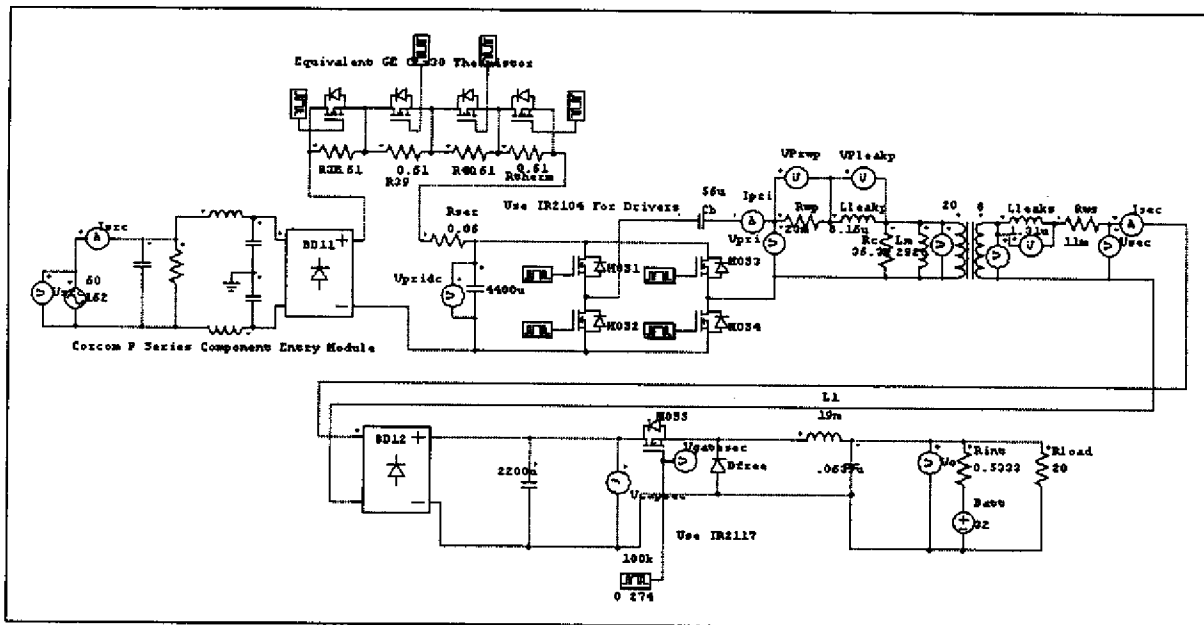


Figure 30: Simulation Circuit: $I_{CHARGE} = 15A$

Figure 31 contains all of the notable current waveforms. Even with the thermistor inserted, it can be seen that the surge current is as high as +55A and as low as -35A. For this

reason, when the circuit was actually built, two thermistors were utilized in a series configuration to further lower the current. The pink waveform is the RMS value of the source current. This value was used to determine which thermistor should be used (using the datasheet). The duty ratio of the buck converter was adjusted to achieve 15A into the battery, the maximum value by procedure for performing a battery charge for the installed Bluefin battery. With the simulated components, the ripple current through the “buck” inductor (L1) is 104 mA.

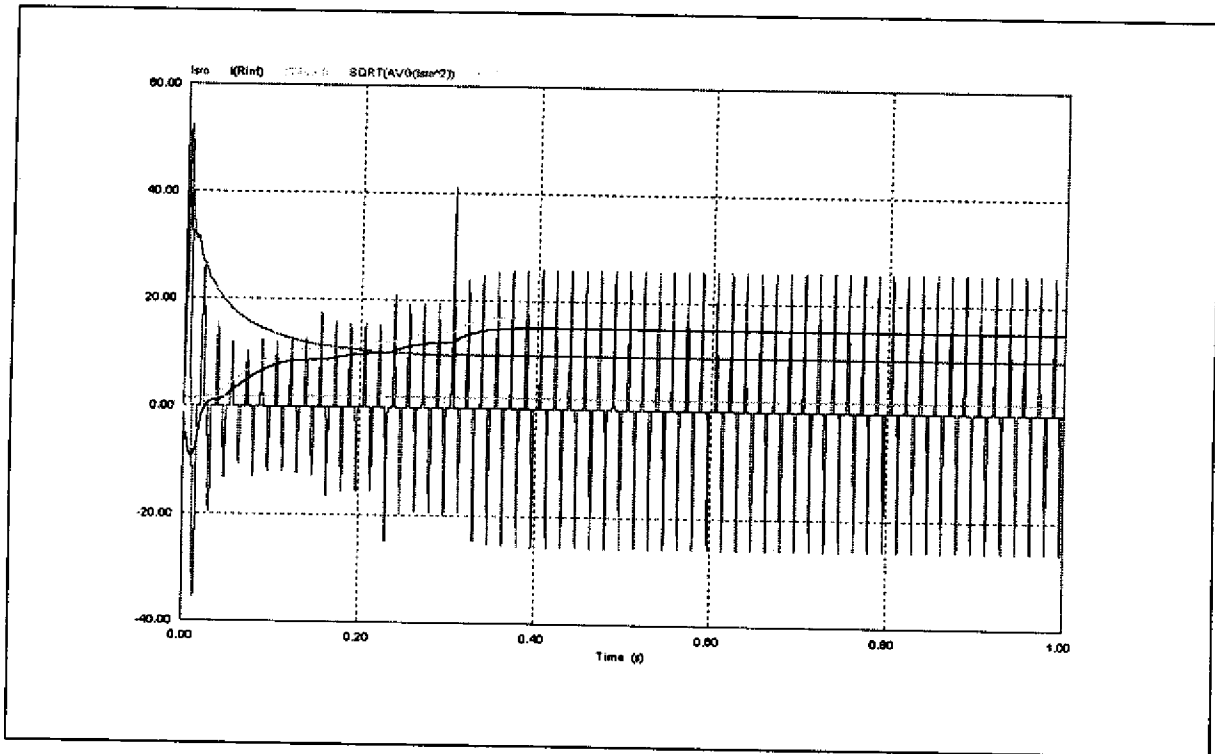


Figure 31: Simulation: $I_{\text{CHARGE}} = 15\text{A}$, $dI_L = 104\text{mA}$, $dI_{\text{CHARGE}} = 102\text{mA}$

Figure 32 shows the voltage waveforms. The top waveform is the “smoothed,” rectified output of the smoothing capacitor on the primary side (the middle waveform is the secondary side DC voltage). The bottom waveform is the output of the “buck” converter. It can not be seen here, but the output voltage ripple is 52 mV.

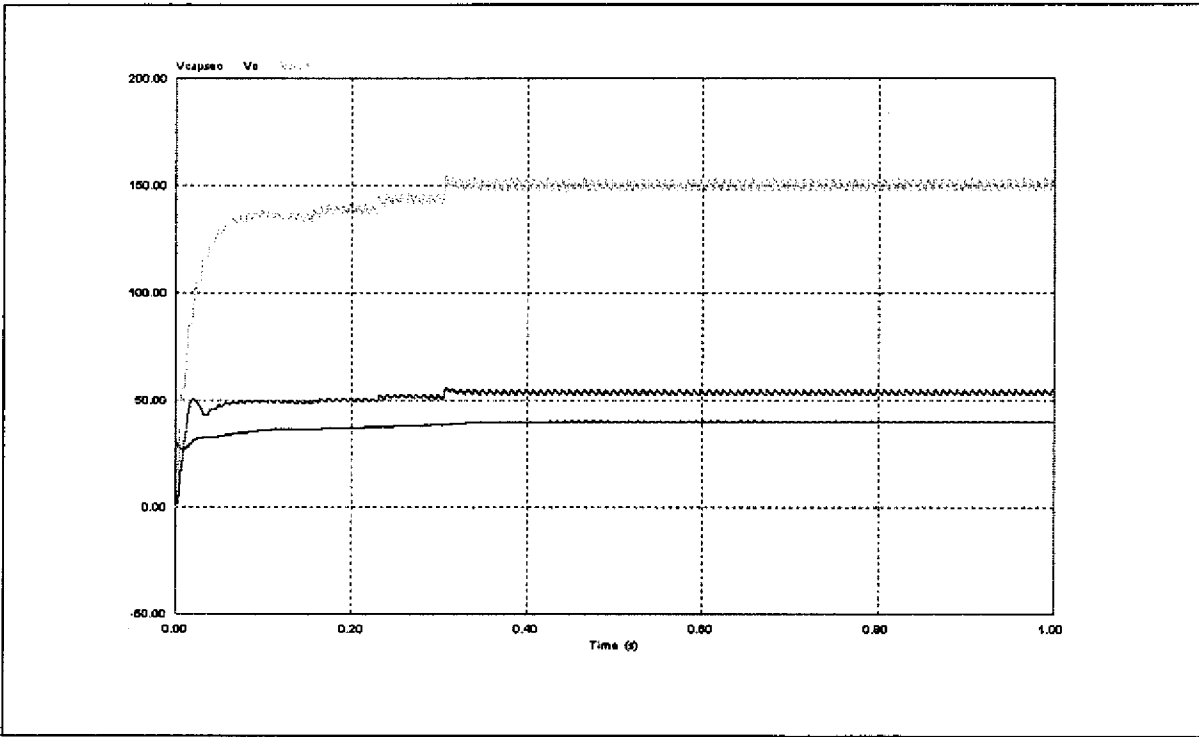


Figure 32: Simulation: $I_{\text{CHARGE}}=15\text{A}$, $dV_{\text{O}}=52\text{mV}$

Chapter 4 Prototype Results

With the background knowledge of the theory and simulation in hand, the circuit could now be prototyped and operated. The circuit was built as shown in Figure 30 with explanatory details to follow.

4.1 Secondary Circuit

The “buck” converter is at its minimum power output when the battery charge is complete. At that time, the only output is the normal AUV loads (2 Amps @ approximately 34 VDC). However, it should also be noted that the period ($1/f_{sw}$, where the switching frequency is 100 kHz) must be maintained much less than the time constant, L/R . Using Equation 9, a series of calculations were made using the commercially available capacitor and inductor values. The minimum value of inductance for the “buck” circuit was determined to be 19mH, which correlates to a capacitor value of 0.0639 μ F. Setting an acceptable value of ripple output voltage, the ripple current was calculated by:

Equation 17

$$di_{out} = \frac{V_{out}(1-d)T}{L_{min}} = 2mA$$

This results in an acceptable value for ripple current.

The built circuit is shown in Figure 33. The self-wound inductor is shown on the top right. A self-wound inductor was used to get a more accurate value of inductance. The bridge rectifier is shown on the bottom left. Directly above the rectifier is the smoothing capacitor (2200 μ F). The three heat sinks are from bottom to top: the MOSFET, the free-wheeling diode and an additional output diode. The output diode was added to prevent the battery from

maintaining the circuit energized when the charging circuit is not in operation. The final piece of the secondary circuit is the driver circuit for the MOSFET (Figure 34).

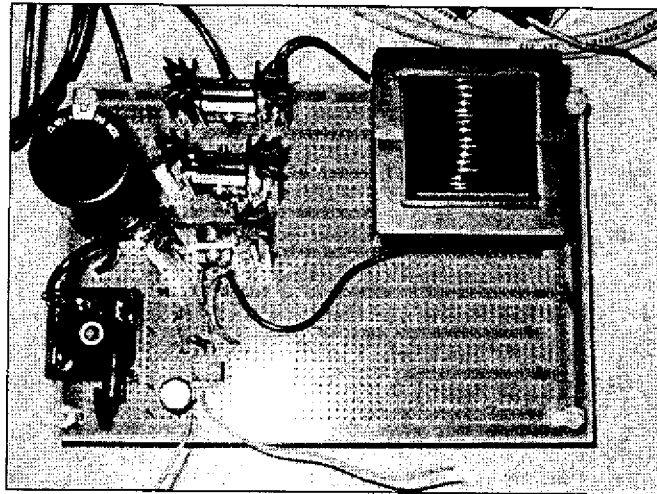


Figure 33: Secondary Circuit

Normally, when the driver circuit is first energized, the bootstrap capacitor (CB) is charged through D1 to ground. However, because this circuit is being used as a battery charger, the potential at the top of D2 (or pin VS) is at battery voltage. This reduces the voltage across the bootstrap capacitor and driver will shut-off on under voltage. Therefore, a resistor (R1) and zener diode (D3) are added to the circuit. The zener diode maintains the top of the bootstrap capacitor at 15 V (depending on the rating of the zener diode) above VS while the bypass resistor provides a path for the bootstrap capacitor to be charged [4].

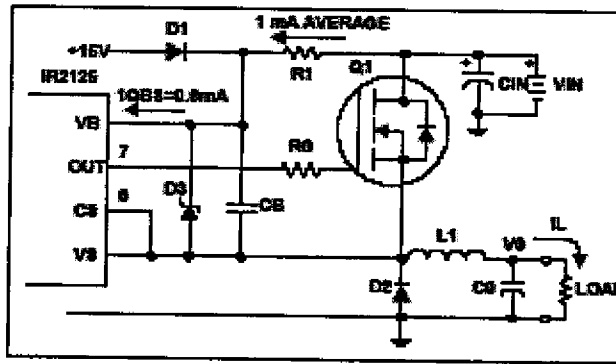


Figure 34: MOSFET Driver Circuitry [4]

The operation of the secondary circuit was verified by applying a DC supply voltage to the smoothing capacitor. A high power resistor was used as the load. An IR2125 driver was used which is 2.5V, 5V and 15V compatible. The driver input voltage was implemented using a function generator and is shown as CH1 in Figure 35. With an input voltage of 6.2 VDC to the “buck” converter and a duty ratio of 50%, the output voltage was 2.26 VDC. The output voltage was measured at the cathode of the output diode. Taking the voltage drop across the diode to be 0.85V (datasheet), this correlates with a 50% duty ratio at 3.11V. CH2 of Figure 35 measures the gate voltage of the MOSFET. With the MOSFET off, the bootstrap capacitor charges to 15V as discussed previously. Once the gate pulse is turned on, freewheeling diode D3 turns off and the 3.11V at the output is immediately sensed at the top of D2. This explains the value of ~18V when the gate pulse is on. CH1 of Figure 36 is the same as Figure 35, but CH2 now measures the output of the “buck” converter. A small ripple can be seen on CH2, and the value is between 2.8 and 3.0V.

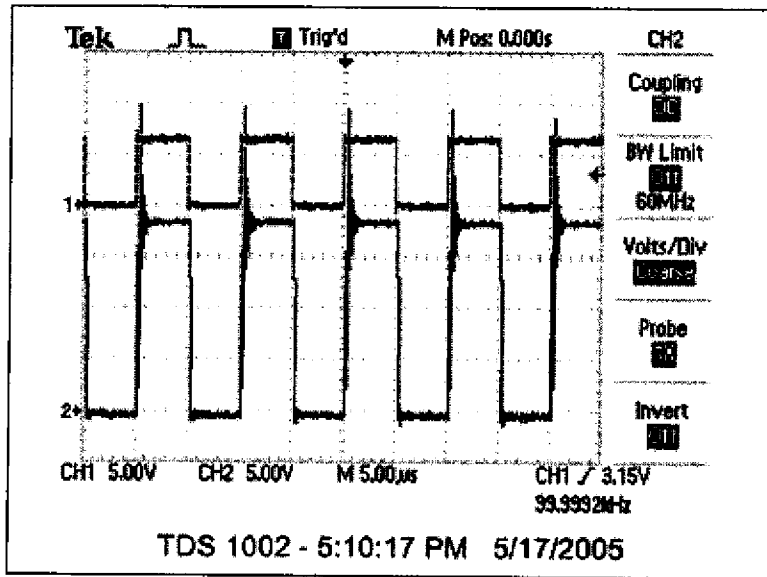


Figure 35: MOSFET Driver Input and Output Waveforms: $V_{in}=6.2\text{VDC}$, $V_{out}=2.26\text{V}$, $d=0.5$

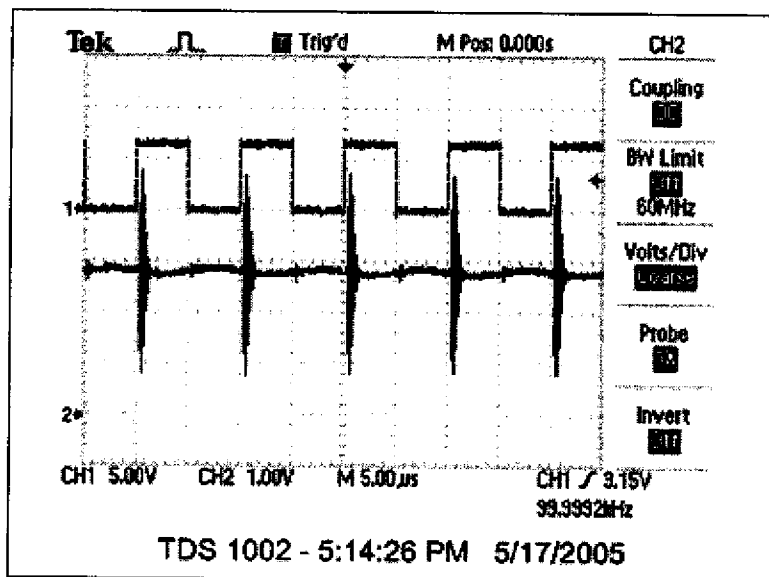


Figure 36: MOSFET Driver Input and "Buck" Converter Output Waveforms: $V_{in}=6.2\text{VDC}$, $V_{out}=2.26\text{V}$, $d=0.5$

By increasing the duty ratio to 80% and the "Buck" converter input to 12.7 VDC, the voltage at the output of the output diode increases to 9.2 V. Again, taking the voltage drop across the diode to be 0.85V, this correlates to a duty ratio of 79%.

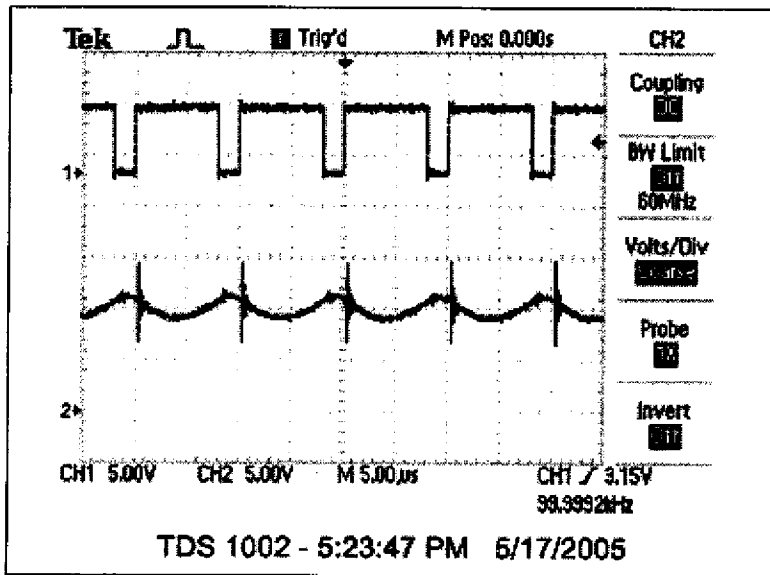


Figure 37: MOSFET Driver Input and "Buck" Converter Output Waveforms: $V_{in}=12.7$ VDC, $V_{out}=9.2$ V, $d=0.8$

4.2 Primary Circuit

The primary circuit, shown in Figure 38, was the last portion to be built. The input to the circuit is on the bottom left-hand corner at the bridge rectifier. The input is fed through the component entry module and has two outputs. The first output is a regulated +/- 12V power converter. The output of the +/- 12V power supply has an option for grounding the positive or negative terminal so that the other output can be used. In this case, the negative terminal was grounded to the negative terminal of the main rectified output. This allows the +12V supply to float at 12V above the negative terminal.

The second output of the component entry module is the bridge rectifier. On the rectified output, the primary smoothing capacitor (top left) maintains a relatively constant voltage to be sent to the H-bridge (top right). The H-bridge is driven by two half-bridge drivers (bottom right,

next to the red lead). The H-bridge uses a 555 timer to set the switching frequency (20 kHz), with the 555 timer being fed to each half-bridge driver. Referring to Figure 30, MOS1 and MOS2 are driven by one half-bridge driver and MOS3 and MOS4 are driven by the second driver. The difference between the inputs to the two drivers is that the second gets an inverted 555 timer output. This is done to ensure there is no direct (short) path for the rectified output from positive to negative rail. CH1 of Figure 39 is the first driver high output and CH2 is the second driver high output.

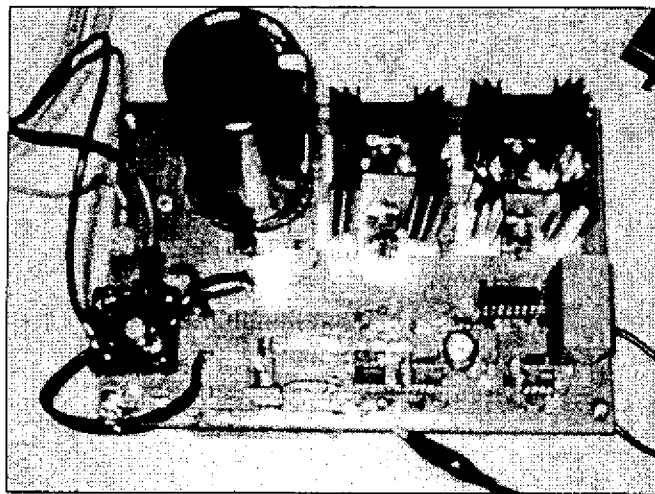


Figure 38: Primary Circuit

To test the circuit operation, the inductive coupler was connected across the output of the H-bridge. On the secondary side of the inductive coupler, a load resistor (5.6Ω) was connected across the output. The coupler and load were connected to guarantee the H-bridge had an acceptable supply and return path to ensure the driver circuitry operated properly. Once the primary was energized, the differential voltage across the load resistor was measured and is shown in Figure 40. In the figure, M is the difference between CH1 and CH2. In addition, a

voltmeter reading was taken across the load resistor and read 67 Vac, which is consistent with the expected value based on the coupler turns ratio (20/8).

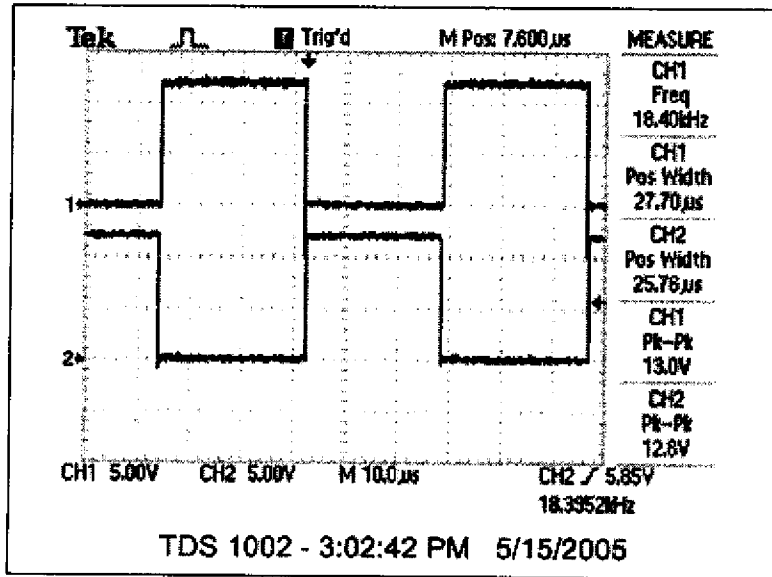


Figure 39: Primary MOSFET Driver High Output

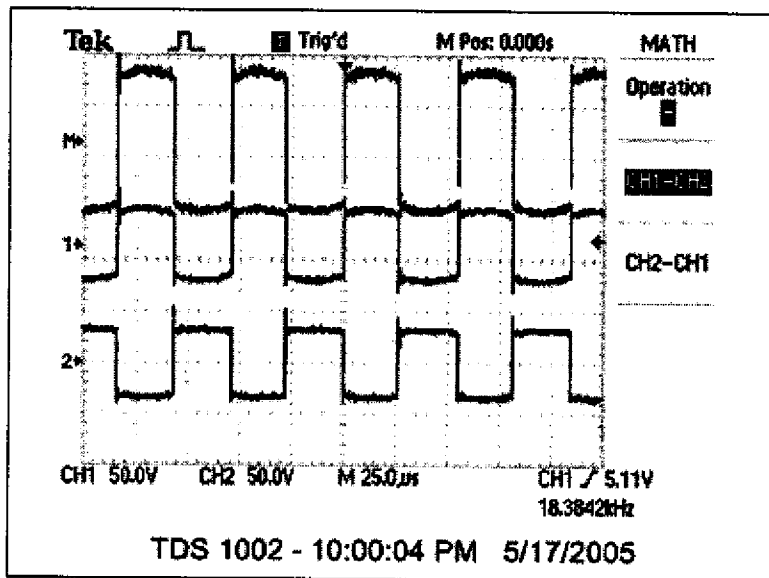


Figure 40: Inductive Coupler Output (M = CH1 - CH2)

Chapter 5 Conclusions

Overall, the simulated and actual circuits performed consistently with each other. The Lithium-ion Polymer battery is very sensitive to fluctuations in the charge current and voltage. Referring to Figure 37, it is possible that the voltage ripple for the actual circuit is too high and some modifications may need to be made to the “buck” converter. Specifically, the “buck” converter’s inductor and output capacitor may need to vary in an attempt to further minimize the ripple voltage and current, thus minimizing the risk of damage to the battery.

The circuit was designed to be as simple as possible. There are some modifications which were considered, but not implemented due to time constraints. These modifications should make the circuit more efficient. The recommended modifications are:

- Add a snubber circuit to each MOSFET. A snubber circuit is used to control the voltage and/or current in the MOSFET (or any switch) during the transition period from on to off and vice versa. Chapter 24 of [5] contains basic information for implementing this circuit.
- Utilize interleaved power conversion techniques to increase the effective ripple frequency presented to filter elements while reducing the net ripple through harmonic cancellation. An excellent source for this concept is “Interleaved Power Conversion Techniques for High Density Power Supplies,” by Brett Miwa (MIT PhD Thesis, 1992).
- Implement an inductive coupler which does not have to manually be connected. For example, there is work currently in progress to use a portion of the hull of the AUV as the means for transformer coupling.

Acknowledgements

The author would like to thank the following for their contribution in completing this thesis:

- MIT Sea Grant College Program for funding this project under Grant # NA16RG2255.
- Professor Chrysostomos Chrysostomidis for your patience and persistence.
- Professor Jim Kirtley for the knowledge, persistence and dedication in making this design work.
- Sam Dasset, Jim Morash, Victor Polidoro and Rob Damus for their many hours spent in the lab and answering all the “dumb” questions. Thank you for your patience.
- Professor Steven Leeb for your last minute intuition.

List of References

[1] ANSI/IEEE Std 390-1987 "An American National Standard: IEEE Standard for Pulse Transformers," Electronics Transformer Technical Committee of the IEEE Magnetics Society, May 1987.

[2] L. A. Gish, "Design of an AUV Recharging System," MIT Thesis for Naval Engineer and Master of Science in Oceans Systems Management, June 2004.

[3] B. J. Heeres, D. W. Novotny, D. M. Divan, and R. D. Lorenz, "Contactless Underwater Power Delivery," 25th Annual IEEE Power Electronics Specialists Conference, PESC '94 Record, Vol.1, pp. 418-423, June 1994.

[4] "International Rectifier AN978-b: HV Floating MOS-Gate Driver ICs," [Online document, available <http://www.irf.com>, 2003, [cited May 2, 2005].

[5] J. G. Kassakian, M.F. Schlecht, G.C. Verghese, "Principles of Power Electronics," Addison-Wesley Publishing Company, Inc., 1991.

[6] "Magnetics: A Critical Comparison of Ferrites with Other Magnetic Materials," [Online document, available <http://www.mag-inc.com/pdf/cg-01.pdf>, 2000, [cited Oct. 26, 2004].

[7] "Magnetics: Ferrite Cores Design Manual and Catalog [E, I, U, EEM, EFD Cores (Section 11)]," [Online document, available http://www.mag-inc.com/pdf/2004_E_I_U_EEM_EFD_Cores.pdf, 2000, [cited Oct. 26, 2004].

[8] "Magnetics: Ferrite Cores Design Manual and Catalog [Power Design (Section 4)]," [Online document, available http://www.mag-inc.com/pdf/2004_Design_Information.pdf, 2000, [cited Oct. 26, 2004].

[9] "Magnetics: Material Information," [Online document], available http://www.mag-inc.com/pdf/2004_Materials.pdf, 2004, [cited Oct. 26, 2004].

[10] S. Rhodes, J.L. Kirtley, and S.B. Leeb, "The Effects of Separable Cores on High Power Transformer Design," MIT Thesis, August 1996.

[11] L. Van den Steen, "Inductive Couplers in Underwater Power Distribution Networks – Improving Their Applicability," Underwater Technology, Vol.12 Number 3, pp. 3-9 and 16, Autumn 1986.